OPTIMAL COLLIMATOR DESIGN USING MONTE CARLO SIMULATION AND RSM FOR BREAST SCINTIGRAPHY

by

BARIŞ BİLGİN

B.S., Mechanical Engineering, Yıldız Technical University, 2002

Submitted to Institute of Biomedical Engineering

in partial fulfillment of the requirements

for the degree of

Master of Science

in

Biomedical Engineering

Boğaziçi University

June 2006

ACKNOWLEDGEMENTS

I would like to thank to my thesis supervisor Assoc. Prof. Dr. Albert Güveniş for his extraordinary support, and patience. His assistance and advices were invaluable for me. I also would like to thank to Assoc. Prof. Michael Ljungberg for his help with SIMIND.

Also thanks to my family for their support.

ABSTRACT

OPTIMAL COLLIMATOR DESIGN USING MONTE CARLO SIMULATION AND RSM FOR BREAST SCINTIGRAPHY

Scintimammography can be a useful adjunct to physical examination and mammography for the detection and characterization of breast tumors, especially for patients with dense breast tissue, architectural distortion of the breast, breast implant or with equivocal mammography. However, one major limitation of Scintimammography is its poor sensitivity and image quality for small lesions (<1.5cm). The aim of this work is to optimize the collimator parameters of a Scintimammography system to achieve better image quality by using Monte Carlo Simulation and the Response Surface Method.

Two software packages have been used for this purpose: SIMIND is a Monte Carlo Simulation program developed by Dr. Michael Ljungberg. NCSS is a statistical analysis software package used for the Response Surface Method (RSM). Monte Carlo has a wide usage in nuclear medicine imaging, however RSM has not been used much in this area. RSM stems from science disciplines in which experiments are performed to study the unknown relation between a set of variables and the system output, or response. We ran SIMIND to simulate a planar gamma camera system and carry out the experiments. NCSS was used for the optimization process. The SNR (signal-to-noise ratio) is selected as the detectability index. A MATLAB program was written to compute SNR values from the outputs of SIMIND. The breast was modeled as a cylinder full of water and a spherical lesion with a diameter of 0.3 cm. Our results show that for a constant septa size of 0.02 cm, we can obtain optimum detectability when the diameter is 0.132 cm and collimator length is 1.449.

Keywords: *Scintimammography, Monte Carlo simulations, Response Surface Methods, Collimator Optimization*

ÖZET

GÖĞÜS SİNTİGRAFİSİ İÇİN MONTE CARLO SİMÜLASYONU VE TYM KULLANILARAK OPTIMAL KOLİMATÖR TASARIMI

Sintimamografi; özellikle kalın göğüs dokusu, göğüste form bozukluğu, takma göğüs ve şüpheli mamografi vakalarında, fiziksel muayene ve mamografiye ek olarak göğüs tümörlerinin tespit edilmesinde ve tanımlanmasında yararlı olabilir. Sintimamografinin en önemli dezavantajı ise küçük lezyonlardaki (<1.5cm) düşük hassasiyeti ve görüntü kalitesidir. Bu çalışmanın amacı, Monte Carlo Simülasyonu ve Tepki Yüzey Metodunu kullanarak bir Sintimamografi sisteminin kolimatör parametrelerini optimize edip daha iyi görüntü kalitesi elde etmektir.

Bu amaçla iki yazılım kullanılmıştır: SIMIND, Dr. Michael Ljungberg tarafından geliştirilen bir Monte Carlo simülasyon programıdır. NCSS ise Tepki Yüzey Metodu (TYM) için kullanılan bir istatistiksel analiz yazılım paketidir. Monte Carlo nükleer tip görüntülemede yaygın olarak kullanılmaktadır, fakat TYM bu alanda pek fazla kullanılmamıştır. TYM, değişkenler ve sistem çıkışı (ya da tepki) arasındaki bilinmeyen bağıntıları çözmek için deneyler yapılan bilim dallarından çıkmıştır. Düzlemsel gamma kamera sistemini simüle etmek ve deneyleri yapmak için SIMIND çalıştırdık. Optimizasyon işlemi için ise NCSS kullanıldı. SNR (Sinyal-gürültü oranı), algılama indeksi olarak seçildi. SIMIND çıkışlarını SNR değeri olarak hesaplayacak bir MATLAB programı yazıldı. Göğüs su dolu bir silindir ve 0.3 cm çaplı küresel bir lezyon olarak modellendi Sonuçlarımıza göre 0.02 cm septa ölçüsü için 0.132 cm çap ve 1.449 kolimatör uzunluğu ile optimum tespit edilebilirliğe ulaşılır.

Anahtar kelimeler: *Sintimamografi, Monte Carlo Simülasyonu, Tepki Yüzey Metodları, Kolimatör Optimizasyonu*

LIST OF FIGURES

LIST OF TABLES

LIST OF SYMBOLS

Re	Spatial resolution
ε	Efficiency
N	Particle histories
W	Particle history weight
c	Contrast
η	Response surface

LIST OF ABBREVIATONS

RSM	Response Surface Method
DOE	Design of experiments
SPECT	Single-Photon Emission Tomography
PET	Positron Emission Tomography
MRI	Magnetic Resonance Imaging
CT	Computed Tomography
PMT	Photomultiplier tube
PHA	Pulse Height Analyzer
FOV	Field of view
RNG	Random number generator
SG	Simple geometry
SB	Shape-based
VB	Voxel-based
SNR	Signal-to-noise ratio
SD	Standard deviation

1. INTRODUCTION

1.1 Background and Motivation

Nearly 75–80 percent of breast biopsies instigated by mammographic findings are benign on histopathologic examination. Other imaging modalities such as MRI, ultrasound and Scintimammography are employed to compensate for these deficiencies in mammography [1]. Scintimammography is used for problem solving in difficult cases, such as dense breasts and architectural distortion of the breast. However, one major limitation of Scintimammography is its poor sensitivity and image quality for small lesions (<1.5 cm) [2].

1.2 Objectives

One way of achieving better image quality would be optimizing the collimator parameters such as hole diameter, hole length and septal thickness, which play a crucial role determining the image quality. Our aim in this project will be finding the optimum values for the hole diameter and the hole length variables using Monte Carlo simulation and RSM for maximum lesion detectability in breast scintigraphy.

G.H. Simmons et. al. [3] was one of the first studies to conduct a parallel-hole collimator optimization using a non-linear programming method in 1975. Several research projects have been conducted for the same purpose using Monte Carlo simulation. Gengsheng L. Zeng et. al. and Grant T. Gullberg et. al. [4] made a feasibility study using reconstructed images to design a parallel-hole low-energy collimator by changing hole diameter as a variable. Sain et. al. [5] used computer simulation, a phantom model and a detectability index in order to evaluate a planar camera for breast scintigraphy. There are also studies comparing resolution and sensitivity advantages of pinhole and parallel-hole collimators for Scintimammography.

Response Surface Methodology (RSM) is one of the designs of experiments (DOE) methods used to approximate an unknown function for which only a few values are computed. The RSM stems from science disciplines in which physical experiments are performed to study the unknown relation between a set of variables and the system output, or response. The RSM method has a wide usage in many industries for designing robust products but has not been used much in nuclear imaging area. In our Project we will be using this method for optimizing.

1.3 Outline

Chapter 1 introduces the subject, presents the motivation of the thesis and gives an outline. Chapter 2 is a brief explanation of breast scintigraphy imaging techniques. The Monte Carlo method used in this thesis is discussed in Chapter 3. It gives information about Monte Carlo techniques used in nuclear medicine and software packages for this purpose. Chapter 4 presents the detectability index used in this thesis, SNR. Response Surface Method is discussed in Chapter 5. Chapter 6 includes the materials and a summary of the basic results. Chapter 7 is the conclusion of the proposed thesis.

2. BREAST SCINTIGRAPHY AND INSTRUMENTATION

2.1 Breast Scintigraphy (Scintimammography)

Breast scintigraphy is a functional imaging technique whereby radionuclide tracers in the patient's breasts are observed with a gamma camera (SPECT). Tracers are designed to accumulate in tumors more than in healthy tissue. Scintimammography is not intended as a breast cancer screening procedure, however, it is a reliable technique used in the patient with breast cancer. Breast scintigraphy images are complementary to mammography, ultrasound and magnetic resonance imaging. The nuclear medicine images are reported in conjunction with the patient's previous studies from one or more of these modalities [1,6].

Scintimammography is indicated in the selection of mammographic abnormalities for biopsy; in the evaluation of patients with dense breasts and scarring related to a previous surgery, in which evaluation with conventional mammography is difficult; and in the detection of regional lymph node metastases [1,6].

The radiopharmaceutical used for breast imaging is 99mTc sestamibi, originally developed for myocardial perfusion imaging. Although the exact mechanism of 99mTc-MIBI uptakes in tumors is unknown, it is believed that it is primarily taken up in tumor cells due to its lipophilic nature, which permits passive transport through the tumor membranes and is actively taken up by mitochondria once inside the cell. Cells with higher mitochondrial activity will have greater concentration of 99mTc-sestamibi [6].

After the injection of the tracer in the patient's body, with the patient in the prone position, the breast is suspended and separated from the chest wall, ensuring the breast that is not being imaged is out of the field of view. Special foam pads are commercially available to accommodate imaging the patient in this position. Because axillary lymph node chains are the major regional drainage sites for the breast, a supine image ensuring both axilla are included is also performed. Before the study is submitted for reporting, the technologist ensures the results of the physical examination and all adjunct modality images are available for the nuclear medicine physician [6,7].

Below are two Scintimammogram images; the subject of the first image is a 45-year-old female with a suspicious mass, on screening mammogram (not shown) in the right breast. Scintimammogram (shown) demonstrates a focal area of intense increased uptake in the region corresponding to the abnormality on the mammogram. Histopathology demonstrates a 1.3 cm invasive ductal carcinoma. In the second image, the subject is a 42-year-old female with extremely dense breasts on mammogram (not shown) with no visible abnormality. Physical exam reveals two masses in the right breast in the upper/outer and lower/inner quadrant. Scintimammogram (shown) of the right breast demonstrates a focal intense area of increased uptake in the upper portion of the right breast corresponding to physical exam. The lower/inner quadrant lesion shows normal uptake. Histopathology of both lesions shows a 2 cm infiltrating ductal carcinoma of the upper lesion and fibroadenoma of the lower/inner lesion [1].

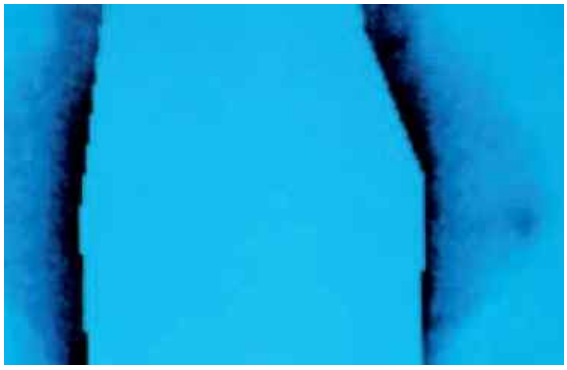

Figure 2.1 Scintimammogram image of a 45-year-old patient [1]

Figure 2.2 Scintimammogram image of a 42-year-old patient with dense breasts [1]

2.1.1 Instrumentation for Breast Scintigraphy

A single- or multiple-head gamma camera is needed to acquire planar and/or tomographic (SPECT) images. This gamma camera should be equipped with a low energy, high-resolution collimator. An imaging table (mattress) with specially designed breast cutouts to allow the breast to be fully dependent or with a foam cushion with a lateral semicircular aperture is required. The energy window for image collection should be 10% (±5%) centered over the 140-keV photopeak of 99mTc [6].

2.1.2 Gamma Camera

Gamma Camera was developed in the 1950s and 1960s, before PET, x-ray CT or MRI. Like PET, it bases its information on the concentration of radionuclides present in the body. Gamma Camera produces a 3D image by rotating a photon detector around the body and gaining information from different angles, as in CT. The emission source in this case is injected into the body.

2.1.2.1 The Imaging Process

1. The Imaging Process Starts with Radioactive Emissions from a Source:

Gamma Camera works by using radioactive tracers, injected into the body, to visualize organs in the body. These radioactive tracers are radionuclides that emit a single photon (with about 140kEV), unlike PET, which emits positrons, and results in 2 high-energy 511 keV photons. This radioactive tracer is almost always Technetium. (Technetium 99 Emits Gamma Rays (140 keV), Chemistry of molecule allows for easy bonding, the half-life is 6 hours which is ideal: long enough to take accurate measurements, short enough not to cause extensive damage.)

The radioactive tracer has to be injected into the body, usually through the blood stream through what is called a radiopharmaceutical, which is a precise mixture of the source isotope and a biogenic carrier. The tracer emits a low Energy Gamma Ray that can easily pass through the human body and into the detector without causing the patient any pain.

2. The image collection begins with the Camera Collimator:

Unlike with PET, Gamma Camera photon detection is done using a collimator in a technique known as collimation. A collimator is a metal block (such as lead or tungsten), containing many tiny holes, placed between the body and the radiation detector. These holes are long and narrow, allowing only parallel photons to pass through to reach the detector and rays that stray slightly to be absorbed by the lead. If the orientation of the collimator, and therefore the holes, is known, the original path of detected photon is linearly extrapolated.

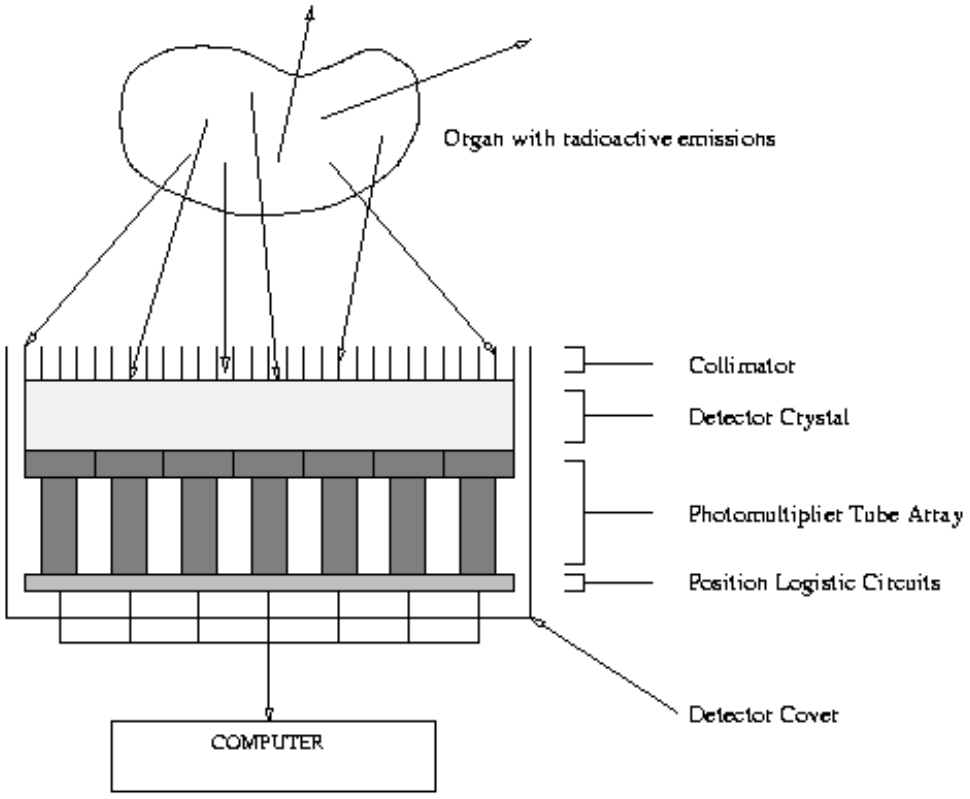

Figure 2.3 Gamma Camera system [8]

3. The real detection is performed in the Detection Crystal:

The Scintillation material used is usually Sodium Iodide, which we know, is one of the easier crystals to grow but is still very expensive. In the detector the crystals are shaped into discs or rectangles with a thickness of about 1 cm. Within the Crystal, the initially ejected gamma ray goes through either the Photoelectric Effect or Compton

Scattering. In both of the situations, scintillation event occurs, in which light is emitted. PMTs situated along the posterior crystal face detect this light and amplify it. The crystal is fragile and must have an aluminum housing that protects it from moisture, extraneous light, and minor physical damage.

4. The Photomultuplier tubes:

The light that is given off by the scintillation process is very minimal. To magnify the signals, a bank of photomultiplier tubes is used. The PMT array performs 2 specific functions: it converts the light image into an image of electrical pulses, and it amplifies the intensity of the image. PMT also detects where each gamma photon is absorbed in the crystal.

A scintillation event occurring in the crystal is recorded by one or more PMTs. Localization of the event in the final image depends on the amount of light sensed by each PMT and thus on the pattern of PMT voltage output. Weighing the output of each tube then forms the summation signal for each scintillation event. This signal has three components spatial coordinates on X and Y-axes as well as a signal (Z) related to intensity. The X and Y coordinates may go directly to instrumentation for display on the CRT or may be recorded in the computer. The PHA then processes the signal intensity.

5. Pulse Height Analyzer (PHA):

The basic principle of the PHA is to discard signals from background and scattered radiation or radiation from interfering isotopes, so that only photons known to come from the photopeak of the isotope being imaged are recorded. The PHA discriminates between events occurring in the crystal that will be displayed or stored in the computer and events that will be rejected.

Signal intensity information is matched in the PHA against an appropriate window, which is really a voltage discriminator. To allow energy related to the desired isotope photopeak to be recorded, the window has upper and lower voltage limits that define the window width. A %20 symmetric window for 140-keV photopeak means that the electronics will accept 140 ± 14keV gamma rays. Any signals higher or lower than this are rejected.

6. Imaging:

The data collection can be done with any standard computer. The hardware requirements are very minimal for today's standards but the software involved is expensive.

There are various Imaging Techniques. They differ mainly in the position of the camera but they all use very similar techniques. Some examples are:

- Planar
- Planar Dynamic
- SPECT
- Gated SPECT [8,9].

2.2 Collimators

The purpose of the collimator is to project an image of gamma rays onto the surface of the camera crystal. Holes are positioned in the collimator so that each point on the crystal's surface has a direct view only of one point on the surface of the target. In effect, each point of the crystal is able to see only the radiation originating from a corresponding point on the patient's body.

Collimators play a crucial role in defining a systems extrinsic imaging characteristics. The energy rating of a collimator indicates the maximum energy of photons that can be efficiently handled by the collimator. This is usually defined as the energy at which less than 5% of the off-axis photons pass through the collimator. Low energy collimators are designed for a maximum energy of 140 to 200 keV, while medium energy collimators are effective up to 300-400 keV. The energy rating of the collimator also dictates septal thickness. Although tungsten absorbs photons more efficiently, most collimators are made of lead due to its lower cost.

There are broadly four types of collimators: parallel hole, converging, diverging, and pinhole. We will be using parallel-hole collimator for imaging the breast. There are also slant hole and fan-beam collimator types [9,10].

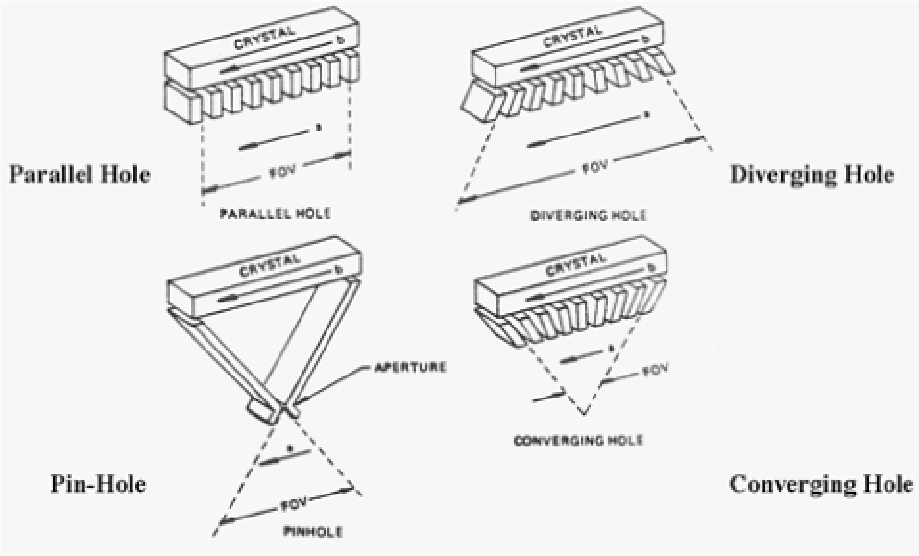

Figure 2.4 Images of different types of collimators [9]

2.2.1 Resolution and Sensitivity

The differences among the collimators are the thickness, number, and size of the holes and the way they are oriented. This, in turn, has an effect on the camera sensitivity, FOV (Field of View) image magnification, and image blur.

Resolution and sensitivity of a collimator are inversely related. The best spatial resolution is achieved with collimators with long holes of a small diameter because the angle of acceptance is smaller and more scatter is rejected. Sensitivity, or efficiency, refers to the fraction of emitted photons, which actually pass through the collimator and reach the detector. The sensitivity increases as the square of the hole size, and decreases as the square of the hole length. Thus, collimator resolution improves as:

- The diameter of the collimator holes decreases
- The effective length of the collimator holes increases
- The object to collimator distance decreases [9,10].

Collimator septa play a crucial effect on the resolution and sensitivity of the camera. Longer septa in the collimator attenuate most photons, except those exactly

perpendicular to the crystal face. This increase in selectivity increases the resolution and decreases the count rate detected. Shortening the length of the septa allows more photons to reach the crystal; thus, the count rate is higher. The spatial resolution is decreased because the photons coming through a hole in the collimator are from a larger area.

2.2.2 Parallel hole Collimators

A common arrangement is for the collimator holes to be parallel, as illustrated in figure 2.4. The FOV is determined by the size (diameter) of the crystal and remains the same at all source-to-camera distances. The size of the image at the crystal is the same as the actual size of the radioactive source being imaged. This relationship does not change with distance. Therefore, the parallel-hole collimator does not produce either magnification or minification of the image. The photons that pass through the parallel-hole collimator are the ones moving in a direction parallel to the holes. Assuming there is no photon absorption between the source and collimator, the number of these parallel photons does not change significantly with the source-to-camera distance. Therefore, camera sensitivity with a parallel-hole collimator is generally not affected by changing the distance between the source and camera [9,10].

The thickness of the collimator, the orientation and size of the holes as well as the distance between source and collimator define the resolution and sensitivity of the camera.

For a parallel-hole collimator the spatial resolution Re is determined by the hole length L, the hole diameter d, and the source to collimator distance z:

$$R_e = \frac{d.(L+z)}{L} \tag{2.1}$$

Looking at the equation 2.1, we can see that a decrease in z and d improves the spatial resolution, while the length of the collimator holes is less influential (typically determined by the thickness of the collimator material necessary to absorb gamma radiation) [4].

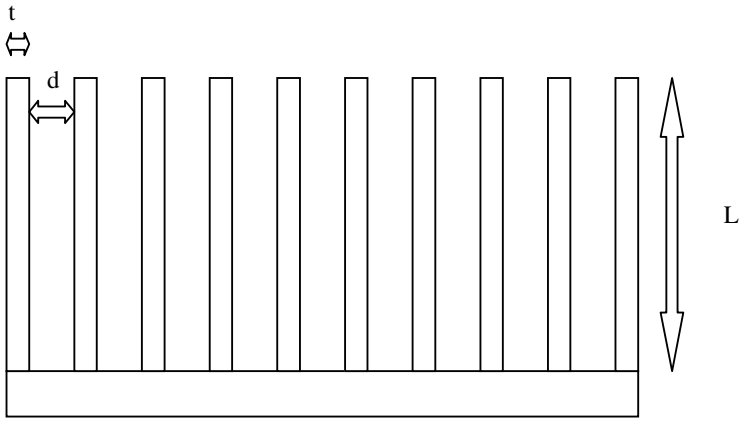

Figure 2.5 Parallel Hole Collimator where t is the septal thickness, d is the hole size, and L is the hole length

The collimator plane source sensitivity is defined as the response of the collimator to an infinite plane source of radioactivity located in the object plane. In the case of cylindrical parallel-hole multi-channel collimators used with a scintillation camera, the total plane source sensitivity S is given by:

$$S \approx d^4 / L^2 a^2 \tag{2.2}$$

Where d is the radius of the collimator hole, L is the hole length and a is the distance between centers of adjacent holes [3].

3. THE MONTE CARLO METHOD

Numerical methods that are known as Monte Carlo methods can be loosely described as statistical simulation methods, where statistical simulation is defined in quite general terms to be any method that utilizes sequences of random numbers to perform the simulation. Monte Carlo methods have been used for centuries but only in the past several decades has the technique gained the status of a full-edged numerical method capable of addressing the most complex applications. The name Monte Carlo was chosen during the World War II Manhattan Project because of the close connection to games based on chance and the location of a very famous casino in Monte Carlo [11].

Monte Carlo techniques have become one of the most popular tools in different areas of medical physics following the development and subsequent implementation of powerful computing systems for clinical use. In particular, they have been extensively applied to simulate processes involving random behavior and to quantify physical parameters that are difficult or even impossible to calculate analytically or to determine by experimental measurements. The applications of the Monte Carlo method in medical physics cover almost all topics, including radiation protection, diagnostic radiology, radiotherapy and nuclear medicine, with an increasing interest in exotic and new applications, such as intravascular radiation therapy, boron neutron capture therapy and synovectomy [11, 12]

3.1 Principles

The general idea of Monte Carlo analysis is to create a model, which is as similar as possible to the real physical system of interest, and to create interactions within that system based on known probabilities of occurrence, with random sampling of the probability density functions (PDFs). As the number of individual events (called histories) is increased, the quality of the reported average behavior of the system improves, meaning that the statistical uncertainty decreases. Assuming that the behavior of the imaging system can be described by probability density functions pdf's, then the Monte Carlo simulation can proceed by sampling from these pdf's, which necessitates a fast and effective way to generate random numbers uniformly distributed on the

interval. Photon emissions are generated within the phantom and are transported by sampling from pdf's through the scattering medium and detection system until they are absorbed or escape the volume of interest without hitting the crystal. The outcomes of these random samplings, or trials, must be accumulated or tallied in an appropriate manner to produce the desired result, but the essential characteristic of Monte Carlo is the use of random sampling techniques to arrive at a solution of the physical problem [13,14].

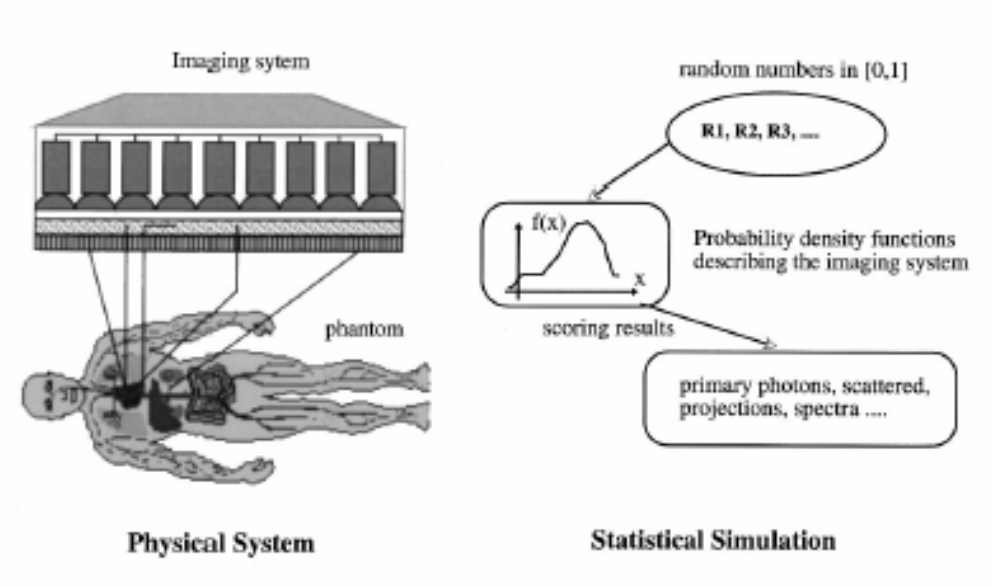

Figure 3.1 Principles of Monte Carlo simulation of an imaging system [14]

The primary components of a Monte Carlo simulation method include the following;

i) Probability density functions (pdf's) : the physical system must be described by a set of pdf's.

ii) Random number generator: a source of random numbers uniformly distributed on the unit interval must be available.

iii) Sampling rule: a prescription for sampling from the specified pdf's.

iv) Scoring: the outcomes must be accumulated into overall tallies or scores for the quantities of interest.

v) Error estimation: an estimate of the statistical error (variance) as a function of the number of trials and other quantities must be determined.

vi) Variance reduction techniques: methods for reducing the variance in the estimated solution to reduce the computational time for Monte Carlo simulation.

vii) Parallelization and vectorization algorithms to allow Monte Carlo methods to be implemented efficiently on advanced computer architectures [14].

3.1.1 Random Number Generation

Random number generation is a key issue for the Monte Carlo Method, which is used to estimate true random events. Monte Carlo methods make extensive use of random numbers to control the decision-making when a physical event has a number of possible results.

Random number generators (RNG) are based upon specific mathematical algorithms so that they have the appearance of randomness but nevertheless exhibit a specific repeatable pattern. A large number of generators are readily available, and many of these are suitable for the implementation on any computer system. A typical simulation uses from 107 to 1012 random numbers, and subtle correlations between these numbers could lead to significant errors. The largest uncertainties are typically due more to approximations arising in the formulation of the model than those caused by the lack of randomness in the RNG.

The sequence of random numbers used to affect a Monte Carlo model should possess some properties. The sequences of random numbers should be serially uncorrelated. The generator should not repeat; practically, the repetition should occur only after the generation of a very large set of random numbers. The sequence of random numbers should be uniform, and unbiased. The generation of the random

numbers should be fast and reproducible. Linear congruential and Lagged –Fibonacci generators are the most commonly used generators [11,14].

3.1.2 Analog Sampling

Analog Monte Carlo attempts to simulate the full statistic development of the electromagnetic cascade. If we assume that a large number of particle histories, N, are included in a batch, the individual batch estimates can be considered as drawn from a normal distribution. For a given calculation, the estimated uncertainty is proportional to the inverse of the square root of the number of histories simulated. The efficiency ε of a Monte Carlo calculation can therefore be defined as;

$$\varepsilon = \frac{1}{\sigma^2 T^2} \tag{3.1}$$

where T is the calculation time to obtain a variance estimate σ2. For large N, ε should be constant as long as the calculation technique remains the same.

As described earlier, the imaging system can be described in terms of pdf's. These pdf's, supplemented by additional computations; describe the evolution of the overall system, whether in space, energy, time or even some higher dimensional phase space. The goal of the Monte Carlo method is to simulate the imaging system by random sampling from these pdf's and by performing the necessary supplementary computations needed to describe the system evolution. In essence, the physics and mathematics are replaced by random sampling of possible states from pdf's that describe the system. Thus, it is frequently necessary to sample some physical event, the probability of which is described by a known pdf. Let x be the physical quantity to be selected and f(x) the pdf. Among the properties of the pdf is that it is integrable and non-negative. Assume that the domain of f(x) is the interval $[x_{min}, x_{max}]$ and that it is normalized to unit area. The cumulative distribution function F(x) of the frequency function f(x) is defined as;

$$F(x) \equiv probability(\tau \leq x) = \int_{x_{\min}}^{x} f(\tau) d\tau \qquad (3.2)$$

A stochastic variable can be sampled by the use of uniformly distributed random numbers R in the range [0–1] using one of the techniques described below [14,15].

3.1.2.1 Direct Method

This method can be used if the inverse of the cumulative distribution function F-1(x) is easily obtainable. Since F(x) is uniformly distributed in [0–1], the sampled value of x could be obtained by substituting F(x) in equation 3.2 by a uniform random number R, that is, x = F-1(R). A practical example of using this technique is the calculation of the distance to the next interaction vertex. The inversion is not always possible, but in many important cases the inverse is readily obtained [14].

3.1.2.2 Rejection Method

Another method of performing this when it is too complicated to obtain the inverse of the distribution function is to use the rejection technique, which follows the following steps: (i) define a normalized function f I(x) = f(x) / fmax(x), where fmax(x) is the maximum value of f(x) ; (ii) sample two uniformly distributed random numbers R1 and R2; (iii) Calculate x using the equation x = xmin + R1 (xmax – xmin); and (iv) if R2 is less than or equal to f I(x), then x is accepted as a sampled value; otherwise a new value of x is sampled.

Over a large number of samples, this technique will yield a set of values of x within the required distribution. It does, however, require two random numbers per trial and many trials may be required depending on the area under of the curve of f(x). A typical example of using this technique is the photon energy and scattering angle resulting from incoherent scattering [14].

3.1.2.3 Mixed Methods

When the previous two methods are impractical, the mixed method that combines the two may be used. Assume that the pdf can be factored as follows: f(x) = h(x)g(x), where h(x) is an invertible function and g(x) is relatively flat but contains most of the

mathematical complexity. The method consists of the following steps: (i) normalize *h(x)* producing $h^{I}(x)$ such that $\int_{x_{min}}^{x_{max}} h^{I}(x)dx = 1$; (ii) Normalize *g(x)* producing $g^{I}(x)$ such that $g^{I}(x) \leq 1$ for x in $[x_{min}, x_{max}]$; (iii) use the direct method to select an x using $h^{I}(x)$ as the pdf; (iv) use x and apply the rejection method using $g^{I}(x)$, i.e., choose a random number **R**, if $g^{I}(x) \leq \mathbf{R}$, accept x; otherwise go back to step (iii) [14].

3.1.3 Non-analog Sampling (Variance Reduction Techniques)

A direct Monte Carlo simulation using true probability functions may require an unacceptable long time to produce statistically relevant results. Photons emission is isotropic, so directional parameters may be sampled uniformly within their individual ranges. The geometrical efficiency of a low-energy, general purpose collimator is of the order of 10^{-4}. When direct Monte Carlo simulations were applied in this case, then 9999 photons, on the average, would be rejected for each photon passing through a collimator hole, because of the small solid angle defined by the collimator holes. Therefore, the calculation would be very ineffective in terms of required computing time. It is thus desirable to bias the sampling (non-analog sampling) by introducing different types of importance sampling and other variance reduction techniques to improve the computational efficiency of the Monte Carlo method. The results obtained by non-analog simulation are, however, biased by the variance reduction technique and a correction for this is required. A particle history weight, W, is introduced, which describes the probability of the particle following the current path. This weight is calculated for each particle history, and used in the calculation of the results. If an event occurs, the weight W is added to the counter rather than incrementing the counter by one unit. There are many different variance reduction techniques in nuclear medicine [14,16].

3.2 Monte Carlo Techniques in Nuclear Medicine

There has been an enormous increase and interest in the use of Monte Carlo techniques in all aspects of nuclear imaging, including planar imaging, SPECT, PET and multimodality imaging devices. However, due to computer limitations, the method

has not yet fully lived up to its potential. With the advent of high-speed supercomputers, the field has received increased attention, particularly with parallel algorithms, which have much higher execution rates.

The Monte Carlo method is a widely used research tool for different areas of diagnostic nuclear imaging, such as detector modeling and systems design, image correction and reconstruction techniques, internal dosimetry and pharmacokinetic modeling. The method has proven to be very useful for solving complex problems that cannot be modeled by computer codes using deterministic methods or when experimental measurements may be impracticable. The design of SPECT and PET systems using the Monte Carlo method has received considerable attention, and a large number of applications were the result of such investigations. During the past two decades, the simulation of scintillation camera imaging using both deterministic and Monte Carlo methods has been developed to assess qualitatively and quantitatively the image formation process and interpretation and to assist in the development of collimators. Several researchers have also used Monte Carlo simulation methods to study potential designs of dedicated small animal positron tomographs.

Another promising application of Monte Carlo calculations is the development and evaluation of image reconstruction algorithms and correction methods for photon attenuation and scattering in nuclear medicine imaging, since the user has the ability to separate the detected photons into their components: primary events scatter events, contribution of down scatter events, etc. Monte Carlo modeling thus allows a detailed investigation of the spatial and energy distribution of Compton scatter, which would be difficult to perform using present experimental techniques, even with very good energy resolution detectors.

Monte Carlo simulations have been shown to be very useful for the validation and comparative evaluation of image reconstruction techniques. Smith et al. used Monte Carlo modeling to study photon detection kernels, which characterize the probabilities that photons emitted by radioisotopes in different parts of the source region will be detected at particular projection pixels of the projection images for the case of parallel-hole collimators. The authors also proposed a reconstruction method using 3-D kernels, in which projection measurements in three adjacent planes are used simultaneously to

estimate the source activity of the centre plane. The search for unified reconstruction algorithms led to the development of inverse Monte Carlo (IMC) reconstruction techniques. The principal merits of IMC are that, like direct Monte Carlo methods, the method can be applied to complex and multivariable problems, and variance reduction procedures can be applied [11, 12, 14].

3.2.1 Detector Modeling

Monte Carlo simulation of detector responses and efficiencies is one of the areas, which has received considerable attention. The critical component of emission tomography is the scintillation detector. Increased light per gamma ray interaction, faster rise and decay times, greater stopping power and improved energy resolution are the desired characteristics. Improvements in these characteristics enable detectors to be divided into smaller elements, thus increasing resolution and minimizing dead-time losses [14].

3.2.2 Imaging Systems and Collimator Design

Monte Carlo Method is widely used for the simulation of gamma camera imaging to assess qualitatively and quantitatively the image formation process and interpretation and to assist development of collimators using deterministic methods and simplifying approximations have been developed mainly to improve speed of operation.

In gamma camera imaging, the choice of collimator involves a compromise between sensitivity and spatial resolution. The proper choice of collimator is especially difficult at the cut-off energy level of low-energy collimators and in multiple tracer studies. The relationships between sensitivity, spatial resolution and septal penetration of a given set of collimators have to be studied. The physicist has to determine which of the available collimators provides superior image quality for a given acquisition time. To that end, in addition to its quantitative clinical applications, Monte Carlo simulation may be a useful research tool for tasks such as evaluating collimator design and optimizing gamma camera motion. The improvement in image quality results from the fact that the increase in resolution is greater than the loss of sensitivity.

Monte Carlo techniques were extensively used to analyze the performance of new collimators design for planar gamma camera, SPECT and PET imaging. Approaches to the collimator optimization problem, as well as more sophisticated ‘‘task-dependent’’ treatments and important considerations for collimators design have been performed. Different types of collimators have been simulated to compare their performances. Pinhole collimation for high-resolution imaging of small organs such as the thyroid has also been studied [12, 14].

3.2.3 Image Reconstruction Algorithms

Monte Carlo simulations have been shown to be very useful for validation and comparative evaluation of image reconstruction techniques since it is possible to obtain a reference image to which reconstructed images should be compared. Different image reconstruction algorithms have been investigated for PET, and SPECT [14].

3.2.4 Attenuation and Scatter Correction Techniques

The presence of scatter and attenuation in the images limits the accuracy of quantification of activity. With no corrections, the uncertainty could be as high as 50–100%. Scatter does not produce major artifacts comparable to attenuation but reduces image contrast by including a low frequency blur in the image. The impact of scatter generally depends on the photon energy, camera energy resolution, and energy window settings, besides the object shape and the source distribution. Many of these parameters are non-stationary which implies a potential difficulty when developing proper scatter and attenuation correction techniques. However, correction for scatter remains essential, not only for quantification, but also for lesion detection and image segmentation. Monte Carlo calculations have been found to be powerful tools to quantify and correct for photon attenuation and scattering in nuclear medicine imaging since the user has the ability to separate the detected photons into their components: primary events, scatter events, contribution of down-scatter events, etc. Monte Carlo modeling thus allows a detailed investigation of the spatial and energy distribution of Compton scatter, which would be difficult to perform using present experimental techniques, even with very good energy resolution detectors.

In gamma camera imaging and SPECT, simulation programs have been used to obtain information on the different processes occurring within the phantom and the detectors. For example, energy pulse-height distribution, point-spread function and the scatter fraction can be obtained. The scattered events in the energy–pulse-height distribution can be separated according to the number of scattering events in the phantom. The scatter fraction is of great importance for quantitative estimation of the scattering contribution. It is defined as the ratio between the number of scattered photons and the total number of photons (scattered and unscattered). Most of the research and development has been concentrated on the scatter compensation required for quantitative SPECT. Floyd used Monte Carlo simulations to validate the basic assumptions underlying the empirical implementation of their scatter subtraction algorithm. Three scatter correction techniques for SPECT have been assessed and compared where scatter coefficients and parameters characteristic of each technique have been calculated through Monte Carlo simulations and experimental measurements for various source geometries [12,14].

3.2.5 Dosimetry and Treatment Planning

There is no doubt that the area where early Monte Carlo calculations in the field have been performed is dosimetry modeling and computations. With many advantages of Monte Carlo method amongst the other dosimetry modeling methods it is widely used for this purpose [14].

3.3 Object Modeling and Software Phantoms

Mathematical descriptions of human bodies and anthropomorphic phantoms are useful in radiation transport calculations. They are widely used in computer calculations of doses delivered to the entire body and to specific organs, and are valuable tools in the design and assessment of image reconstruction algorithms. Software phantoms modeled in imaging situations were historically limited to simple point, rod, and slab shapes of sources and attenuating media. Such simple geometries are useful in studying fundamental issues of scatter and attenuation, but clinically realistic distributions cannot be evaluated by such simple geometries. A precise modeling of the human body

requires appropriate information on the location, shape, density and elemental composition of the organs or tissues.

Object modeling is fundamental for performing photon and electron transport efficiently by means of a Monte Carlo method. It consists of a description of the geometry and material characteristics for an object. The material characteristics of interest include density and energy-dependent cross-sections. The modeling includes simple geometry (SG), shape-based (SB), and voxel-based (VB) approaches. The three approaches use a piecewise uniform distribution of object characteristics to model an object. With the SG model, an object is composed of a simple combination of primitives such as cylinders and spheres. The SB approach represents the boundaries of shapes by mathematical equations. Regular shapes such as sphere, cylinder, rectangular solid, etc. have been used to approximate irregularly shaped regions. The VB approach discretizes an object into tiny cubes (voxels) with uniform characteristics. A union of voxels of the same size thus represents an object.

Extensions of SG and SB models such as the solid geometry-based (SGB) approach includes more primitives (ellipsoids, elliptic cylinders, tapered elliptic cylinders, rectangular solids, and their subsets: half, quarter, and eighth) and uses an inclusion tree data structure to provide relationships between primitives. These extensions provide simple irregular shape modeling. To allow anthropomorphic modeling the composite model, which is an extension to the SGB, approach adds to the primitives a voxelized rectangular solid primitive. An object model based on a combination of modified SG, SB and VB models without restriction in the combination set was also proposed [13,14].

3.3.1 Anthropomorphic Phantoms

Modeling of imaging and other medical applications is best done with phantom models that match the gross parameters of an individual patient. Computerized anthropomorphic phantoms can either be defined by mathematical (analytical) functions, or digital volume arrays. The mathematical specifications for phantoms that are available assume a specific age, height and weight. However, people exhibit a variety of shapes and sizes.

Mathematical phantoms are still evolving and are being constantly improved. The heterogeneity of the body has been taken into account by including soft tissues, bone and lungs with different compositions and densities [14].

3.4 Monte Carlo Computer Codes

Many Monte Carlo programs have been in use in the field of nuclear imaging and internal dosimetry with many of them available in the public domain. EGS4, MCNP, SIMSET, SIMIND, SIMSPECT, and PETSIM are some of the Monte Carlo codes widely used [14].

3.4.1 SIMIND

Many Monte Carlo programs have been in use in the field of nuclear imaging, and internal dosimetry, with many of them available in the public domain. One of these programs is SIMIND that has been developed by Dr. Michael Ljungberg, an associate professor at the Department of Medical Radiation Physics, The Jubileum Institute, Lund University, Sweden.

The SIMIND code simulates a clinical SPECT scintillation camera and can easily be modified for almost any type of calculation or measurement encountered in SPECT imaging, including transmission imaging. The entire code has been written in FORTRAN-90 and includes versions that are fully operational on VAX – VMS, most UNIX platforms and on MS-DOS (Lahey LF90 compiler).

In summary, the code works as follows: photons emitted from simulated decay in the phantom are followed step by step towards the scintillation camera. Since the history of acquired events is not lost as is true in practical imaging, important parameters that are not accessible by measurements (for instance, the numbers of scatter interactions in the phantom for a particular photon history or scatter order, scatter angle, imparted energy etc.) can always be deduced from simulated data.

SIMIND includes an accurate treatment of photon interaction in the phantom, a protecting layer and in the crystal of the detector. The simulation of back scattering from light guides and phomultipliers is also included. Different types of collimators can

be selected. SIMIND can take the advantage of anthropomorphic voxel-based phantoms developed for simulating realistic imaging situations. The SIMIND code has been widely used for collimator design and to evaluate attenuation and scatter correction techniques [13,15,17].

4. SNR AS A DETECTABILITY MEASURE

A Detectability index is needed to compare the outputs of our Monte Carlo simulation program SIMIND. There are several methods for lesion detectability measures and one of those methods is SNR (signal-to-noise ratio). SNR is related to the contrast of the lesion as well as the standard deviation of the background. The contrast for a given lesion is defined to be:

$$contrast = \frac{c_{lesion} - c_{background}}{c_{lesion}} \tag{4.1}$$

where c_{lesion} is the average count density in the lesion's region of interest and $c_{background}$ is the average count density in the background.

The percentage standard deviation depends on count statistics and on the reconstruction method. The percentage standard deviation is defined by:

$$\%SD = \sigma_{background} / c_{background} \tag{4.2}$$

where $\sigma_{background}$ is the standard deviation of the background count density and $C_{background}$ is the average count density in the background.

Then the signal-to-noise ratio (SNR) is defined to be:

$$SNR = contrast / \%SD \tag{4.3}$$

and therefore depends on a combination of scanner geometry, reconstruction algorithms, spatial resolution, and sensitivity [18,19].

In our work we developed a MATLAB program to evaluate simulation measures by the means of SNR [20].

5. RESPONSE SURFACE METHOD

Response Surface Methodology, or RSM, is a collection of mathematical and statistical techniques that are useful for the modeling and analysis of problems in which a response of interest is influenced by several variables and the objective is to optimize this response. For example, suppose that a chemical engineer wishes to find the levels of temperature (x1) and pressure (x2) that maximize the yield (y) of a process. The process yields a function of the levels of temperature and pressure:

$$y = f(x1 + x2) + \varepsilon \tag{5.1}$$

where ε represents the noise or error observed in the response y. If we donate the expected response by $E(y) = f(x1,x2) = \eta$, then the surface represented by

$$\eta = f(x1,x2) \tag{5.2}$$

is called a response surface. The response surface is represented graphically such as in Figure 4.1, where η is plotted versus the levels of x1 and x2.

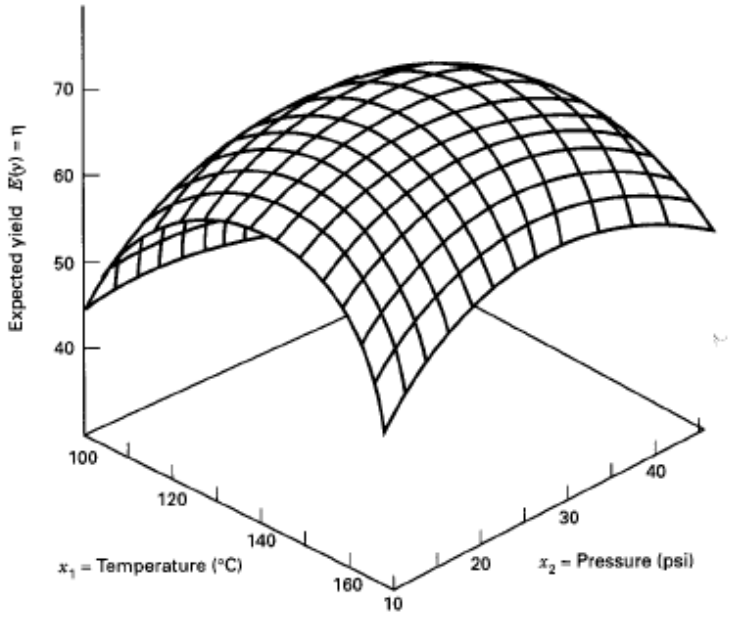

Figure 4.1 A three-dimensional response surface showing the expected yield (η) as a function of temperature (x1) and pressure (x2) [22]

In most RSM problems, the form of the relationship between the response and the independent variables is unknown. Thus, the first step in RSM is to find a suitable approximation for the true functional relationship between y and the set of independent variables. Usually, a low-order polynomial in some region of the independent variables is employed. If the response is well modeled by a linear function of the independent variables, then the approximating function is the first-order model:

$$y = \beta_0 + \beta_i x_i + \beta_2 x_2 + \ldots\ldots\ldots\ldots + \beta_k + x_k + \varepsilon \tag{5.3}$$

If there is curvature in the system, then a polynomial of higher degree must be used, such as the second-order model:

$$y = \beta_0 + \sum_{i=1}^{k} \beta_i x_i + \sum_{i=1}^{k} \beta_{ii} x_i^2 + \sum\sum_{i<j} \beta_{ij} x_i x_j + \in \tag{5.4}$$

where βi, βj, and βij represent regression coefficients; xi, (i = 1….n) are design variables and y is the response.

Almost all RSM problems use one or both of these models. Of course, it is unlikely that a polynomial model will be a reasonable approximation of the true functional relationship over the entire space of the independent variables, but for a relatively small region they usually work quite well.

RSM is a sequential procedure. Often, when we are at appointing on the response surface that is remote from the optimum, there is little curvature in the system and the first-order model will be appropriate. Our objective here is to lead the experimenter rapidly and efficiently along a path of improvement toward the general vicinity of the optimum. Once the region of the optimum has been found, a more elaborate model, such as the second-order model, may be employed, and an analysis may be performed to locate the optimum. As you can see in Figure 4.2, a response surface can be thought of as “climbing a hill,” where the top of the hill represents the point of maximum response.

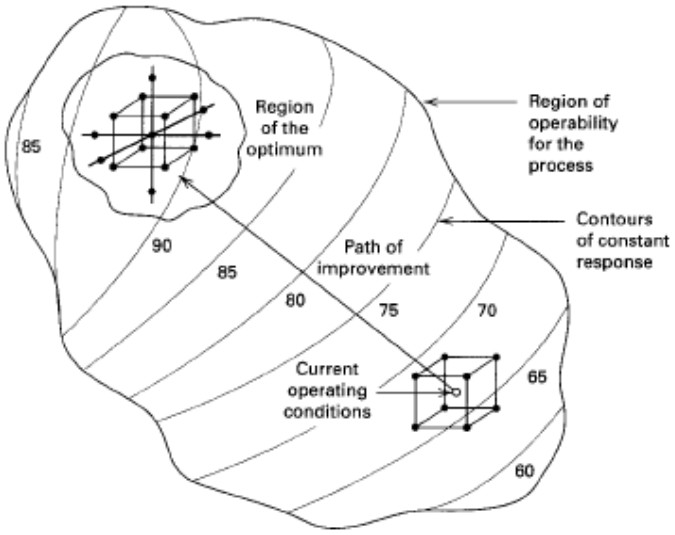

Figure 4.2 The sequential nature of RSM [22]

The eventual objective of RSM is to determine the optimum operating conditions for the system or to determine a region of the factor space in which operating requirements are satisfied [22].

5.1 The Method of Steepest Ascent

In most of the RSM problems, the initial estimate of the optimum operating conditions for the system is far from the actual optimum. In such circumstances, the objective of the experimenter is to move rapidly to the general vicinity of the optimum. When we are remote from the optimum we usually assume that a first-order model is an adequate approximation to the true surface in a small region of the x's.

The method of the steepest ascent is a procedure for moving sequentially along the path of steepest ascent, that is, in the direction of the maximum increase in the response. Of course, if minimization is desired, then we call this technique the method of the steepest descent. The fitted first-order model is:

$$y = \beta_0 + \sum_{i=1}^{k} \beta_i x_i \tag{5.5}$$

and the first-order response surface, that is, the contours of y, is a series of parallel lines such as that shown in Figure 4.3. The direction of the steepest ascent is the direction in which y increases most rapidly. This direction is parallel to the normal to the fitted response surface. We usually take as the path of steepest ascent the line through the center of the region of interest and normal to the fitted surface. Thus, the step along the path is proportional to the regression coefficients (βi). The experimenter based on process knowledge or other practical considerations determines the actual step size.

Experiments are conducted along the path of steepest ascent until no further increase in response is observed. Then a new first-order model may be fit, a new path of steepest ascent determined, and the procedure continued. Eventually, the experimenter will arrive in the vicinity of the optimum. This is usually indicated by lack of fit of a first-order model. At that time additional experiments are conducted to obtain a more precise estimation at the optimum.

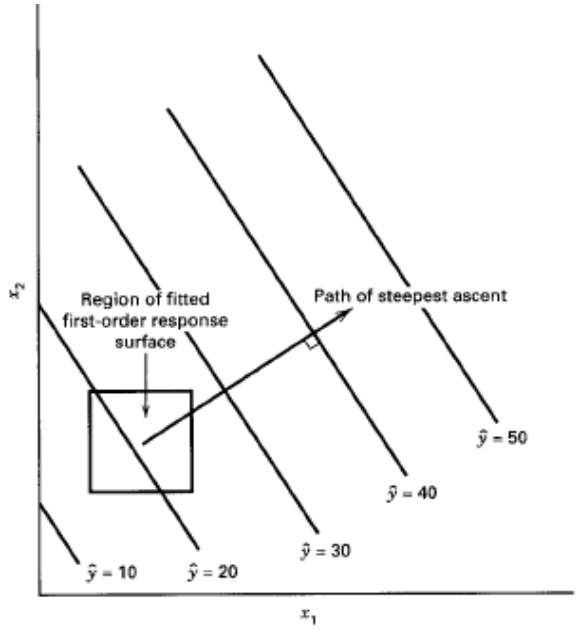

Figure 4.3 First-order response surface and path of steepest ascent [22]

Contour plots play a very important role in the study of the response surface. By generating contour plots using computer software for response surface analysis, the experimenter can usually characterize the shape of the surface and locate the optimum with reasonable precision [22].

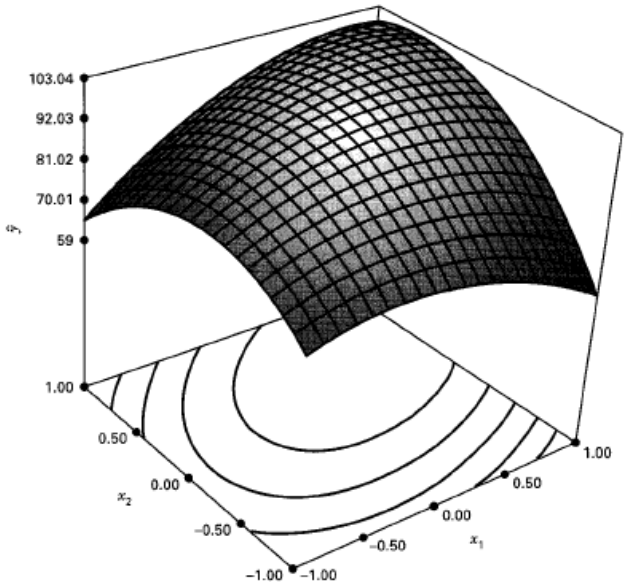

(a) Response Surface

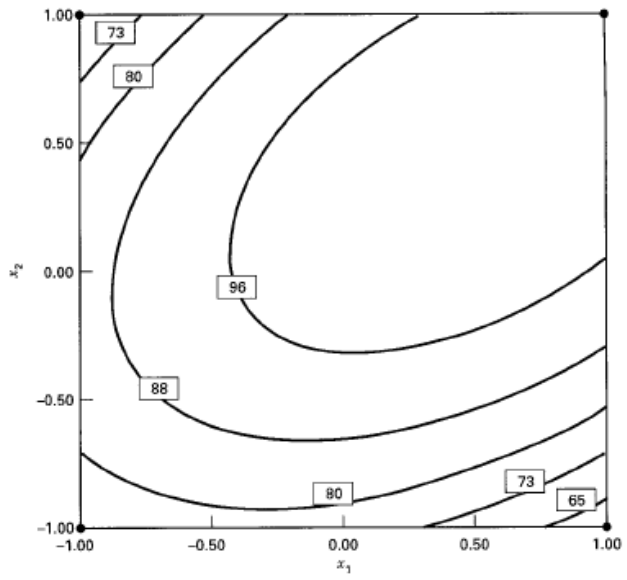

(b) Contour Plot

Figure 4.4 Response surface and contour plot illustrating a surface with a maximum [22]

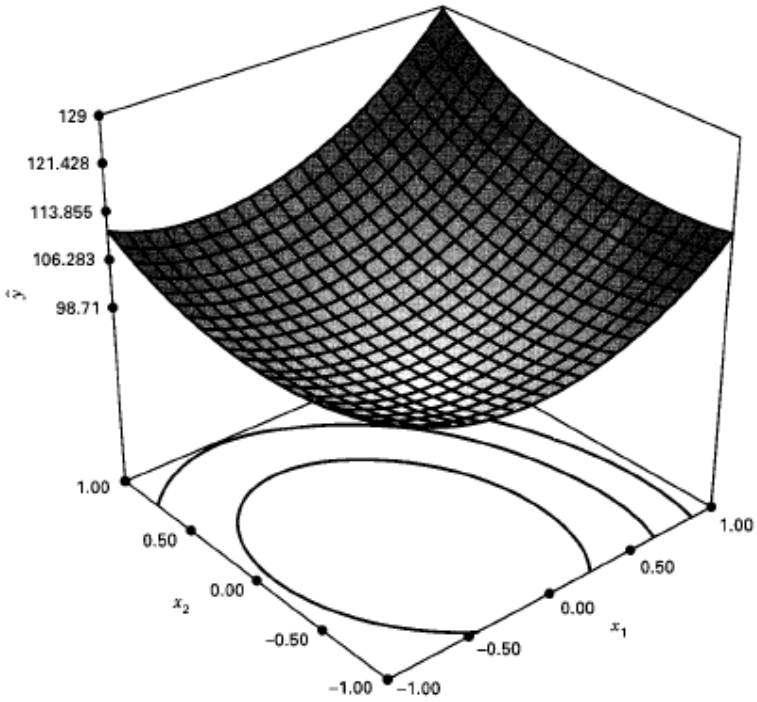

(a) Response Surface

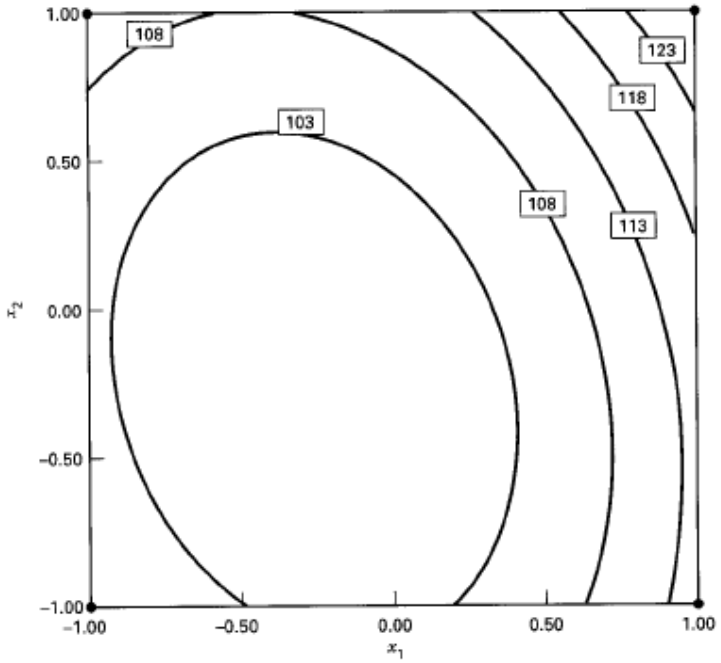

(b) Contour Plot

Figure 4.5 Response surface and contour plot illustrating a surface with a minimum [22]

5.2 Experimental Designs for Fitting Response Surfaces

Fitting and analyzing response surfaces are greatly facilitated by the proper choice of an experimental design. When selecting a response surface design, some of the features of a desirable design are as follows:

i) Provides a reasonable distribution of data points (and hence information) throughout the region of interest

ii) Allows model adequacy, including lack of fit, to be investigated

iii) Allows experiments to be performed in blocks

iv) Allows designs of higher order to be built up sequentially

v) Provides an internal estimate of error

vi) Provides precise estimates of the model coefficients

vii) Provides a good profile of the prediction variance throughout the experimental region

viii) Provides reasonable robustness against outliers or missing values

ix) Does not require a large number of runs

x) Does not require too many levels of independent variables

xi) Ensures simplicity of calculation of the model parameters [22].

These features are sometimes conflicting, so judgment must often be applied in design selection. There are different designs for fitting first-order and second-order models. Central composite design and Box-Behnken designs and their variations are mostly used for fitting response surfaces.

5.3 NCSS Statistical Analysis Software

One of the computer software's for statistical analysis methods is NCSS, which is written by Jerry Hintze. NCSS covers many different analysis methods including Response Surface methods. With NCSS, it is possible to create experimental designs for fitting response surfaces and compute ANOVA reports, which is the statistical technique for testing differences among group means. NCSS draws grid plots for the given experimental values, which helps us to track our way along the maximum. NCSS has also an estimation section for the optimum independent values (x_1, x_2), the values, which makes yield value maximum.

6. METHODS AND MATERIALS

The methodology of my proposed thesis works as follows:

- Creating designs of experiments using NCSS: An interval is determined and two factors are written in the datasheet of NSCC. NCSS computes these values and builds a design of experiments using Central-Composite designs.

- Simulating those experiments via SIMIND: A planar gamma camera system is simulated via SIMIND with collimator parameters varying according to the calculated design of experiments. Two different simulations are made; one for the background and one for the lesion. A binary matrix image is created by the output of SIMIND (*.bim file).

- Calculating the SNR values with the MATLAB program, using the outputs of SIMIND: Lesion and background outputs are combined using MATLAB and SNR values for each situation is calculated. This program also creates images and gives out an Excel file that shows the distribution of counts at the matrix.

- Computing those SNR values with NCSS to find the optimum collimator values: Once the independent values (length, diameter) and dependent values (SNR) are found, NCSS is used to analyze those values.

6.1 Previous Work

As the gamma camera for breast scintigraphy should be equipped with a low-energy, high-resolution collimator, I have investigated the commercial collimator parameters of this specialty. As a result of my research; d (hole diameter) ranges from 0.15cm to 0.30cm, t (septal thickness) ranges from 0.02cm to 0.03cm and L (hole length) ranges from 2.00cm to 5.00cm. SIMIND does not simulate penetration and that's why the lower the septa is the better SNR values are acquired. That's why we chose septa as 0.02cm as a fixed variable. Septa should not be lower then 0.02cm for 140keV photon energy.

The breast was modeled as a cylinder full of water and a spherical lesion with a diameter of 0.3 cm (Figure 6.1). The lesion is located in the centre of cylinder the shaped breast phantom. The cylinder breast has the diameter of 10 cm and the height of 6 cm. Two different simulations are made for each of the experiments; one for the background, one for the lesion. These two simulations are then added up by the MATLAB program and together they form the modeled phantom.

The radioactivity of the lesion and the background are calculated in order to use with the simulation studies. The volume for the background is 235.5cm^3 and has a radioactivity of 3.7Mbq/cc. On the other hand the volume of the lesion is 0.11304cm^3 and the radioactivity of the lesion is three times the background. The total radioactivity of the background is calculated as 871.35Mbq, total radioactivity of the lesion is calculated as 0.836496Mbq. These values are used while simulating the system.

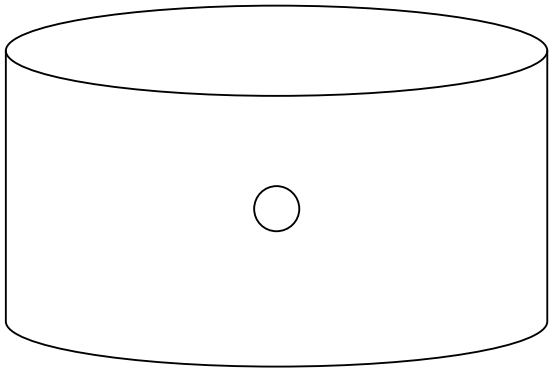

Figure 6.1 Geometry of the simulated phantom

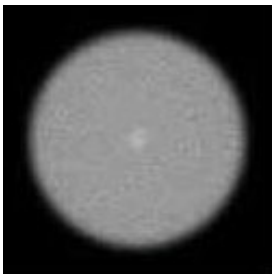

Figure 6.2 Sample image of the simulated phantom

6.2 First Set of Experiments

The first step of the experiments is determining an interval for both diameter and length of the holes. The interval values we choose for our experiments might or might not be the proper values we are looking for. Response Surface Method will guide us to find the proper interval values that makes yield (SNR) maximum. So as a beginning we have chosen 0.10-0.30cm for the diameter and 2.00-4.00cm for the length of the holes for the first set of experiments. Interval values are then computed by NCSS and design of experiments is created. (Table 6.1)

Table 6.1
Design of experiments for the first set of experiments

Ex. #	Hole Diameter	Hole Length
1	0,100	2,00
2	0,100	4,00
3	0,300	2,00
4	0,300	4,00
5	0,059	3,00
6	0,341	3,00
7	0,200	1,59
8	0,200	4,41
9	0,200	3,00
10	0,200	3,00
11	0,200	3,00
12	0,200	3,00
13	0,200	3,00

As we have our design pattern we use SIMIND to carry out the experiments. We simulated two different simulations for lesion, and background and then combined these two simulations' outputs by MATLAB. The simulation parameters are as follows:

Photon energy:	140 keV (99mTc)
Energy resolution:	10.6% at 140 keV
Source dimensions:	0.3x0.3x0.3cm (Sphere)
Phantom dimensions:	5x5x3cm (Cylinder)
Source to detector distance:	4 cm

Energy window:	20%
Pixel size:	0.1 cm (128x128)
Crystal thickness:	0.935
Collimator Hole Shape:	Hexagonal
Simulated photons:	1000000
Simulation time:	600sec

The collimator parameters vary according to the design of experiments and a binary matrix is created as an output of SIMIND (*.bim file) for each situation. The MATLAB program then reads these binary matrixes and SNR values are computed (Table 6.2).

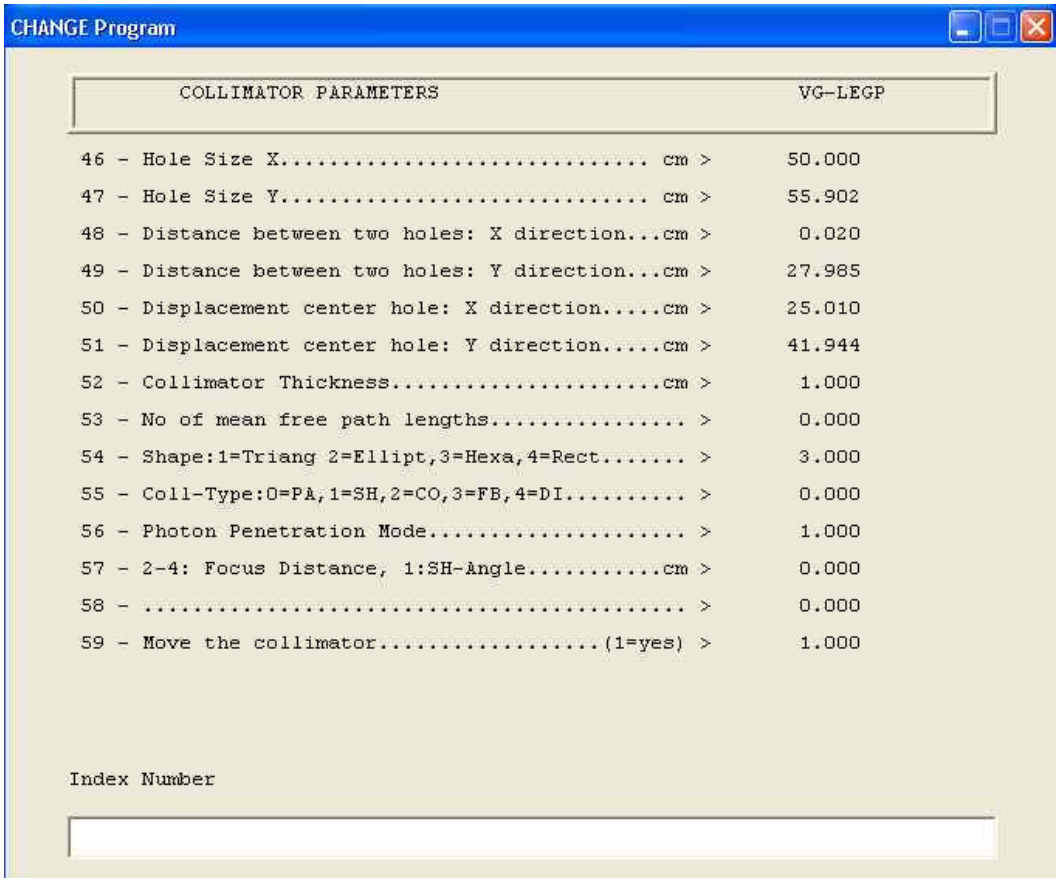

Figure 6.3 A screenshot from the SIMIND program where collimator parameters can be changed

Table 6.2
SNR results of the first set of experiments

Ex. #	Hole Diameter	Septa	Hole Length	SNR
1	0,100	0,02	2,00	7,1278
2	0,100	0,02	4,00	4,3257
3	0,300	0,02	2,00	7,0769
4	0,300	0,02	4,00	7,1127
5	0,059	0,02	3,00	3,2672
6	0,341	0,02	3,00	6,9882
7	0,200	0,02	1,59	7,9632
8	0,200	0,02	4,41	6,5146
9	0,200	0,02	3,00	7,7815
10	0,200	0,02	3,00	7,7509
11	0,200	0,02	3,00	7,6982
12	0,200	0,02	3,00	7,8118
13	0,200	0,02	3,00	7,7455

As explained before, the SNR values found are computed with NCSS. NCSS gives out several reports including ANOVA reports, Estimation report, and Optimum Solution report.

Table 6.3
Sequential ANOVA report of NCSS for the first set of experiments

Sequential ANOVA Section						
		Sequential	Mean		Prob.	Incremental
Source	df	Sum-Squares	Square	F-Ratio	Level	R-Squared
Regression	5	23,9146	4,78292	33,92	0,000092	0,960358
Linear	2	10,88845	5,444226	38,61	0,000166	0,437256
Quadratic	2	11,01273	5,506365	39,05	0,00016	0,442247
Lin x Lin	1	2,013419	2,013419	14,28	0,006905	0,080855
Total Error	7	0,9871532	0,141022			0,039642
Lack of Fit	3	0,9799247	0,326642	180,75	0,0001	0,039352
Pure Error	4	7,23E-03	1,81E-03			0,00029
Sequential ANOVA Section Using Pure Error						
		Sequential	Mean		Prob.	Incremental
Source	df	Sum-Squares	Square	F-Ratio	Level	R-Squared
Regression	5	23,9146	4,78292	2646,7	0	0,960358
Linear	2	10,88845	5,444226	3012,64	0	0,437256
Quadratic	2	11,01273	5,506365	3047,03	0	0,442247
Lin x Lin	1	2,013419	2,013419	1114,15	0,000005	0,080855
Total Error	7	0,9871532	0,141022			0,039642
Lack of Fit	3	0,9799247	0,326642	180,75	0,0001	0,039352
Pure Error	4	7,23E-03	1,81E-03			0,00029

Table 6.3 actually shows two reports. The top is the regular Sequential ANOVA Section defined below. Note that the denominator of the F-Ratios is the Total Error Mean Square. The bottom report is identical to the top, except that the denominator of the F-Ratios is now the Pure Error Mean Square.

This report is designed with two main goals:

1. Determine the sequential influence of the various power and cross-product terms.

2. Test for model lack of fit if repeated observations are available.

Below are the meaning of terms represented at the Sequential ANOVA Report:

Source: The group of independent variables being tested.

Regression: Total of all terms in the model.

Linear: The total for x_i terms.

Quadratic: The total for x_i^2 terms.

Cubic: The total for x_i^3 terms.

Lin x Lin: The total for $x_i x_j$ terms.

Lin x Quad: The total for $x_i x_j^2$ terms.

Quad x Quad: The total for $x_i^2 x_j^2$ terms.

Lin x Cubic: The total for $x_i x_j^3$ terms.

Quad x Cubic: The total for $x_i^2 x_j^3$ terms.

Cubic x Cubic: The total for $x_i^3 x_j^3$ terms.

DF: The degrees of freedom associated with the group of terms.

Sequential Sum-Squares: The regression sum of squares added sequentially by each group of terms. Each group of terms adds this amount of sum of squares after accounting for the terms above it in the report.

Mean Square: The sum of squares divided by the degrees of freedom.

F-Ratio: The F-value formed by dividing the Mean Square by the Total Error Mean Square. Note that these tests are sequential in nature and should be considered from the bottom up. Note that in the second report, the Pure Error Mean Square as the denominator of the F-ratio replaces the Total Error Mean Square.

At Table 6.3, the Lin x Lin F-ratio tests whether the linear-by-linear terms are significant in the regression model after considering the linear and quadratic terms. The Quadratic F-ratio tests whether the quadratic terms add significantly to a model consisting of the linear terms (ignoring the linear-by-linear terms).

Prob. Level: This is the right-tail probability or significance level of this test. Reject the hypothesis that the influence of the terms is zero when this value is less than a predetermined value of alpha, say 0.05.

Incremental R-Squared: The first line displays the total R-Squared for the complete model. The other lines display the amount of R-Squared that is added by each group of terms. Hence, the total of the rest of the lines equals the first.

Lack of Fit and Pure Error: These lines are only displayed if you have repeated observations from which the variability between identical observations may be estimated. The lack of fit tests the adequacy of the specified model. A significant F-test implies that a higher-order polynomial (such as cubic) or a different functional form would fit the data better.

If pure error is available, the F-tests are recalculated using the Pure Error Mean Square as the denominator rather than the Total Error Mean Square.

ANOVA report tests the significance of each factor. Table 6.4 shows two reports. The top is the regular ANOVA Section defined below. Note that the denominator of the

F-Ratios is the Total Error Mean Square. The second report is identical to the top, except that the denominator of the F-Ratios is now the Pure Error Mean Square.

Factor: This line lists the factors being tested for deletion. All terms that include this factor are included in the test. In this occasion C1 and C2 are the factors whereas C1 corresponds to hole diameter and C2 corresponds to hole length.

DF: The degrees of freedom associated with the term(s).

Mean Square: The sum of squares divided by the degrees of freedom.

Table 6.4
ANOVA report of NCSS for the first set of experiments

ANOVA Section						
		Last	Mean		Prob	Term
Factor	df	Sum-Squares	Square	F-Ratio	Level	R-Squared
C1	3	21,00414	7,001381	49,65	0,000044	0,84348
C2	3	5,191391	1,730464	12,27	0,003551	0,208475
Total Error	7	0,987153	0,141022			0,039642
Lack of Fit	3	0,979925	0,326642	180,75	0,0001	0,039352
Pure Error	4	7,23E-03	1,81E-03			0,00029
ANOVA Section Using Pure Error						
		Last	Mean		Prob	Term
Factor	df	Sum-Squares	Square	F-Ratio	Level	R-Squared
C1	3	21,00414	7,001381	3874,32	0	0,84348
C2	3	5,191391	1,730464	957,58	0,000004	0,208475
Total Error	7	0,987153	0,141022			0,039642
Lack of Fit	3	0,979925	0,326642	180,75	0,0001	0,039352
Pure Error	4	7,23E-03	1,81E-03			0,00029

F-Ratio: In the top report, dividing the Mean Square by the Total Error Mean Square forms the F-value. In the second report, dividing the Mean Square by the Pure Error Mean Square forms the F-value. Note that these tests are not sequential, but each tests the importance of the factor after considering all other factors.

Prob Level: This is the right-tail probability or significance level of this test. Reject the hypothesis that the influence of the terms is zero when this value is less than a predetermined value of alpha, say 0.05.

Term R-Squared: The amount that the R-Squared would decrease if this factor were removed from the model.

Lack of Fit / Pure Error: These lines are only displayed if you have repeated observations from which the variability between like observations may be estimated. The lack of fit tests the adequacy of the specified model. If this test is significant, conclude that a higher order polynomial (such as cubic), or a different functional form, would fit the data better.

Table 6.5
Estimation report of NCSS for the first set of experiments

Estimation Section						
Parameter	df	Regression Coefficient	Standard Error	T-Ratio	Prob Level	Last R-Squared
Intercept	1	4,95984				
C1	1	39,24191	8,137042	4,82	0,001916	0,131712
C2	1	-0,81566	0,945916	-0,86	0,417085	0,004211
C1^2	1	-126,295	14,29893	-8,83	0,000048	0,441796
C2^2	1	-0,20103	0,142989	-1,41	0,202549	0,011194
C1*C2	1	7,09475	1,877644	3,78	0,006905	0,080855
Model						
4.95984+ 39.24191*C1-.8156571*C2-126.295*C1^2-.2010316*C2^2+ 7.09475*C1*C2						
Estimation Section Using Pure Error						
Parameter	df	Regression Coefficient	Standard Error	T-Ratio	Prob Level	Last R-Squared
Intercept	1	4,95984				
C1	1	39,24191	0,921123	42,6	0,000002	0,131712
C2	1	-0,81566	0,107079	-7,62	0,001594	0,004211
C1^2	1	-126,295	1,618656	-78,02	0	0,441796
C2^2	1	-0,20103	1,62E-02	-12,42	0,000242	0,011194
C1*C2	1	7,09475	0,212552	33,38	0,000005	0,080855
Model						
4.95984+ 39.24191*C1-.8156571*C2-126.295*C1^2-.2010316*C2^2+ 7.09475*C1*C2						

The report at Table 6.5 shows the regression coefficient estimates of each term and their test of significance. A mathematical model is also created for SNR (yield) in terms of C1 and C2. There are two reports at this table. The top is the regular Estimation Section defined below. Note that the Standard Errors are based on the Total Error Mean Square. The second report is identical to the top, except that the Standard Errors are now based on the Pure Error Mean Square.

Parameter: The particular term being displayed.

DF: The degrees of freedom associated with the term.

Regression Coefficient: The estimated value of the regression coefficient.

Standard Error: The standard error of the above regression coefficient. Note that the Total Error Mean Square is used for the top report, and the Pure Error Mean Square is used for the bottom report.

T-Ratio: The t-value for testing that this regression coefficient is zero after considering all other terms in the model. Note that the Total Error Mean Square is used for the top report, and the Pure Error Mean Square is used for the bottom report.

Prob Level: The probability or significance level of this test.

Last R-Squared: The amount that the R-Squared would decrease if this term were removed from the model.

Table 6.6
Optimum Solution report of NCSS for the first set of experiments

Optimum Solution Section		
	Maximum	Optimum
Parameter	Exponent	Value
C1	2	0,195051
C2	2	1,413165
Function at optimum	8,210601	
Number of Function Evaluations	293	
Maximum Functions Evaluations	500	

This report at Table 6.6 gives the results of the function minimization (or maximization) calculation.

Optimum Value: The value for each of the factors at the computed critical point. Covariates were evaluated at their means.

Function at Optimum: The value of the estimated function evaluated at the optimal values of each of the factors.

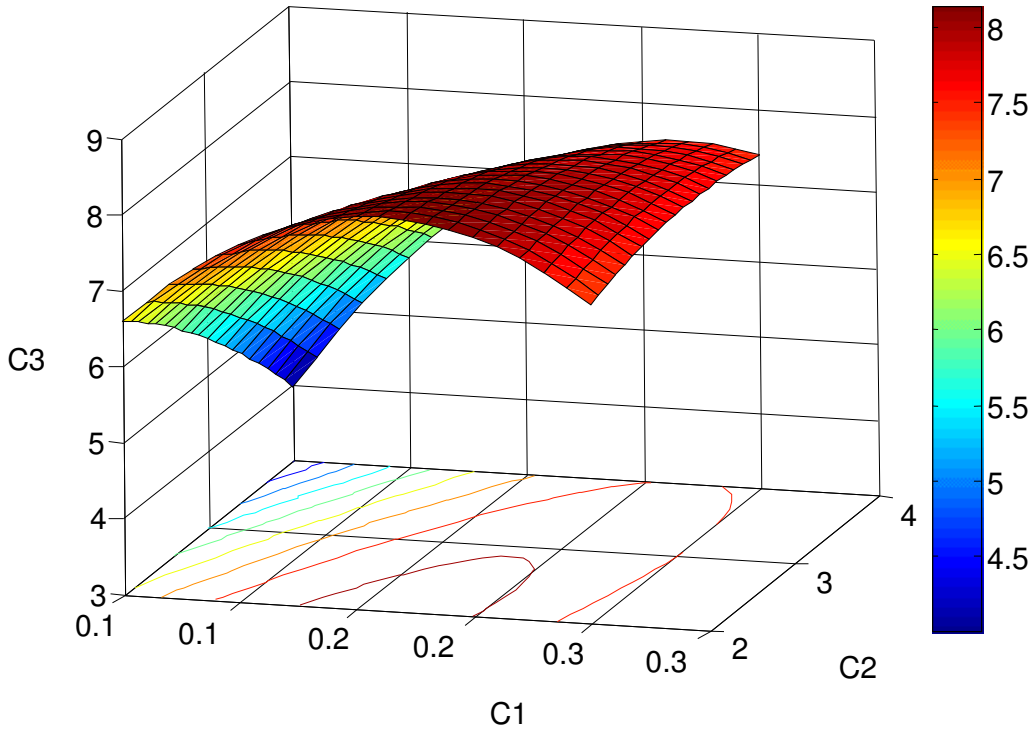

Figure 6.4 Response Surface Plot of C3 for the first set of experiments

6.3 Second Set of Experiments

In figure 6.3 we can see the response surface plot of C3, which is the response of C1 and C2 in our case, SNR. The stationary point shown in the figure, which is a maximum, is not between the intervals we have determined before. That is why we have defined new interval values to carry out the second set of experiments. This time we have chosen 0.15-0.25cm for the hole diameter and 1.00-2.50cm for the hole length of the collimator. We have narrowed the diameter interval and lowered the length interval as NCSS found the optimum value of 1.41cm, which is below the initial interval value.

These values are then computed by NCSS and design of experiments is created for the second set of experiments. (Table 6.7)

Table 6.7
Design of experiments for the second set of experiments

Ex. #	Hole Diameter	Hole Length
1	0,1500	1,0000
2	0,1500	2,5000
3	0,2500	1,0000
4	0,2500	2,5000
5	0,1295	1,7500
6	0,2705	1,7500
7	0,2000	0,6925
8	0,2000	2,8075
9	0,2000	1,7500
10	0,2000	1,7500
11	0,2000	1,7500
12	0,2000	1,7500
13	0,2000	1,7500

SIMIND is then used to carry out the experiments like the first time, and SIMIND's outputs are computed with the MATLAB program (Table 6.8). These values are then computed with NCSS to see ANOVA reports and the grid plot and new optimum values are calculated (Table 6.12).

Table 6.8
SNR results of the second set of experiments

Ex. #	Hole Diameter	Septa	Hole Length	SNR
1	0,1500	0,02	1,0000	7,9670
2	0,1500	0,02	2,5000	7,8026
3	0,2500	0,02	1,0000	6,1008
4	0,2500	0,02	2,5000	7,6770
5	0,1295	0,02	1,7500	8,3907
6	0,2705	0,02	1,7500	7,2660
7	0,2000	0,02	0,6925	5,8030
8	0,2000	0,02	2,8075	7,8157
9	0,2000	0,02	1,7500	8,1652
10	0,2000	0,02	1,7500	8,2310
11	0,2000	0,02	1,7500	8,1226
12	0,2000	0,02	1,7500	8,1779
13	0,2000	0,02	1,7500	7,9948

Table 6.9
Sequential ANOVA report of NCSS for the second set of experiments

Sequential ANOVA Section						
		Sequential	Mean		Prob	Incremental
Source	df	Sum-Squares	Square	F-Ratio	Level	R-Squared
Regression	5	7,561654	1,512331	32,94	0,000101	0,959227
Linear	2	3,868938	1,934469	42,13	0,000125	0,490791
Quadratic	2	2,935294	1,467647	31,96	0,000302	0,372354
Lin x Lin	1	0,757422	0,757422	16,5	0,004801	0,096082
Total Error	7	0,32142	4,59E-02			0,040773
Lack of Fit	3	0,289696	9,66E-02	12,18	0,017653	0,036749
Pure Error	4	0,031724	7,93E-03			0,004024
Sequential ANOVA Section Using Pure Error						
		Sequential	Mean		Prob	Incremental
Source	df	Sum-Squares	Square	F-Ratio	Level	R-Squared
Regression	5	7,561654	1,512331	190,69	0,000076	0,959227
Linear	2	3,868938	1,934469	243,91	0,000066	0,490791
Quadratic	2	2,935294	1,467647	185,05	0,000114	0,372354
Lin x Lin	1	0,757422	0,757422	95,5	0,000614	0,096082
Total Error	7	0,32142	4,59E-02			0,040773
Lack of Fit	3	0,289696	9,66E-02	12,18	0,017653	0,036749
Pure Error	4	0,031724	7,93E-03			0,004024

Table 6.10
ANOVA report of NCSS for the second set of experiments

ANOVA Section						
		Last	Mean		Prob	Term
Factor	df	Sum-Squares	Square	F-Ratio	Level	R-Squared
C1	3	2,492488	0,830829	18,09	0,001119	0,316182
C2	3	5,936042	1,978681	43,09	0,00007	0,753011
Total Error	7	0,32142	4,59E-02			0,040773
Lack of Fit	3	0,289696	9,66E-02	12,18	0,017653	0,036749
Pure Error	4	0,031724	7,93E-03			0,004024
ANOVA Section Using Pure Error						
		Last	Mean		Prob	Term
Factor	df	Sum-Squares	Square	F-Ratio	Level	R-Squared
C1	3	2,492488	0,830829	104,76	0,000295	0,316182
C2	3	5,936042	1,978681	249,49	0,000053	0,753011
Total Error	7	0,32142	4,59E-02			0,040773
Lack of Fit	3	0,289696	9,66E-02	12,18	0,017653	0,036749
Pure Error	4	0,031724	7,93E-03			0,004024

Table 6.11
Estimation report of NCSS for the second set of experiments

Estimation Section						
		Regression	Standard		Prob	Last
Parameter	df	Coefficient	Error	T-Ratio	Level	R-Squared
Intercept	1	7,011738				
C1	1	-7,28086	14,06157	-0,52	0,620566	0,001562
C2	1	2,434231	0,771037	3,16	0,015993	0,058057
C1^2	1	-54,9922	32,63679	-1,68	0,135862	0,016537
C2^2	1	-1,15561	0,145052	-7,97	0,000094	0,369701
C1*C2	1	11,604	2,857103	4,06	0,004801	0,096082
Model						
7.011738-7.280858*C1+ 2.434231*C2-54.99224*C1^2-1.155609*C2^2+ 11.604*C1*C2						
Estimation Section Using Pure Error						
		Regression	Standard		Prob	Last
Parameter	df	Coefficient	Error	T-Ratio	Level	R-Squared
Intercept	1	7,011738				
C1	1	-7,28086	5,843985	-1,25	0,2808	0,001562
C2	1	2,434231	0,320443	7,6	0,001611	0,058057
C1^2	1	-54,9922	13,56385	-4,05	0,015421	0,016537
C2^2	1	-1,15561	6,03E-02	-19,17	0,000044	0,369701
C1*C2	1	11,604	1,187412	9,77	0,000614	0,096082
Model						
7.011738-7.280858*C1+ 2.434231*C2-54.99224*C1^2-1.155609*C2^2+ 11.604*C1*C2						

Table 6.12
Optimum Solution report of NCSS for the second set of experiments

Optimum Solution Section		
	Maximum	Optimum
Parameter	Exponent	Value
C1	2	9,55E-02
C2	2	1,532812
Function at optimum	8,529607	
Number of Function Evaluations	255	
Maximum Functions Evaluations	500	

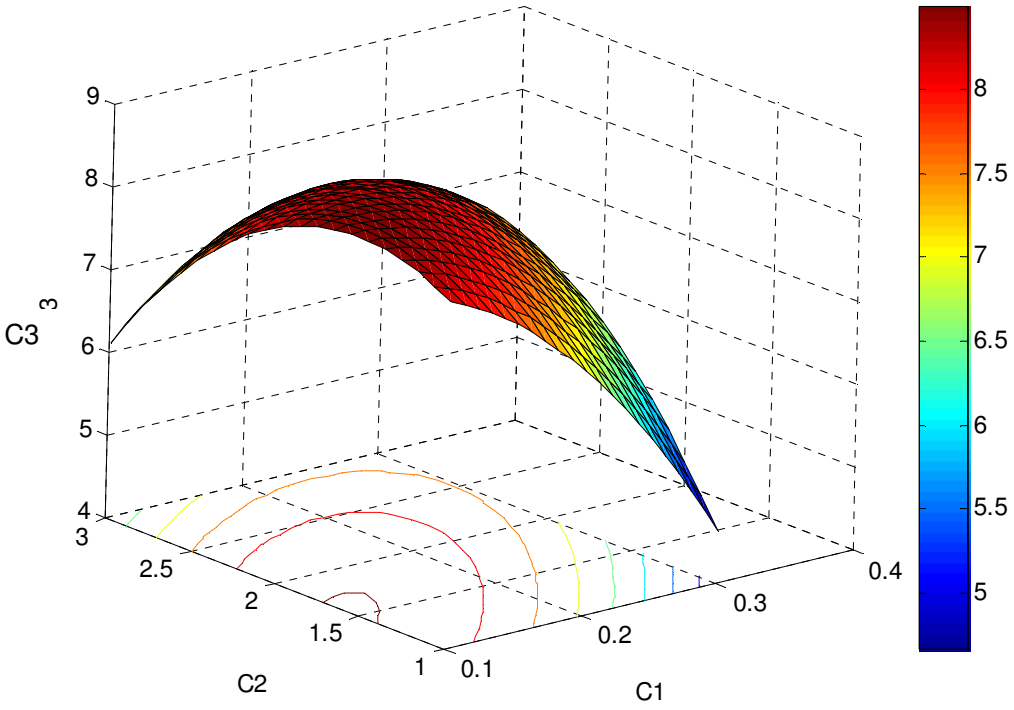

Figure 6.5 Response Surface Plot of C3 for the second set of experiments

6.4 Third Set of Experiments

In the second set of experiments we have seen that, the optimum value for hole length has not changed much but the optimum value for the hole diameter degraded to a value far below our interval. Thus we have defined new interval values, which are: 0.05-0.15cm for the hole diameter and 1.00-2.00cm for the hole length of the collimator. As you see, the diameter interval has been lowered so that we can search the area that the response surface plot indicates as a maximum. Length interval on the other hand has not changed much because we found similar values in both set of experiments. Then, we follow the same path, and these values are computed by NCSS and design of experiments is created for the third set of experiments. (Table 6.13)

Similarly as in the other set of experiments, SIMIND is used to carry out the experiments, and SIMIND's outputs are then computed with the MATLAB program (Table 6.14). After that, these values are computed with NCSS to see ANOVA reports and the grid plot and new optimum values are calculated (Table 6.18).

Table 6.13
Design of experiments for the third set of experiments

Ex. #	Hole diameter	Hole length
1	0,0500	1,000
2	0,0500	2,000
3	0,1500	1,000
4	0,1500	2,000
5	0,0295	1,500
6	0,1705	1,500
7	0,1000	0,795
8	0,1000	2,205
9	0,1000	1,500
10	0,1000	1,500
11	0,1000	1,500
12	0,1000	1,500
13	0,1000	1,500

Table 6.14
SNR results of the third set of experiments

Ex. #	Hole Diameter	Septa	Hole Length	SNR
1	0,0500	0,02	1,000	6,5099
2	0,0500	0,02	2,000	3,8713
3	0,1500	0,02	1,000	7,9099
4	0,1500	0,02	2,000	8,3733
5	0,0295	0,02	1,500	2,6354
6	0,1705	0,02	1,500	8,3323
7	0,1000	0,02	0,795	8,3265
8	0,1000	0,02	2,205	6,7422
9	0,1000	0,02	1,500	8,2328
10	0,1000	0,02	1,500	8,1309
11	0,1000	0,02	1,500	8,1798
12	0,1000	0,02	1,500	8,1019
13	0,1000	0,02	1,500	8,0664

Table 6.15
Sequential ANOVA report of NCSS for the third set of experiments

Sequential ANOVA Section						
		Sequential	Mean		Prob	Incremental
Source	df	Sum-Squares	Square	F-Ratio	Level	R-Squared
Regression	5	40,82332	8,164665	85,99	0,000004	0,98398
Linear	2	26,78139	13,39069	141,03	0,000002	0,645522
Quadratic	2	11,63633	5,818166	61,28	0,000037	0,280475
Lin x Lin	1	2,405601	2,405601	25,34	0,001507	0,057983
Total Error	7	0,664638	0,094948			0,01602
Lack of Fit	3	0,647519	0,21584	50,43	0,001233	0,015607
Pure Error	4	1,71E-02	4,28E-03			0,000413
Sequential ANOVA Section Using Pure Error						
		Sequential	Mean		Prob	Incremental
Source	df	Sum-Squares	Square	F-Ratio	Level	R-Squared
Regression	5	40,82332	8,164665	1907,7	0,000001	0,98398
Linear	2	26,78139	13,39069	3128,77	0	0,645522
Quadratic	2	11,63633	5,818166	1359,43	0,000002	0,280475
Lin x Lin	1	2,405601	2,405601	562,08	0,000019	0,057983
Total Error	7	0,664638	0,094948			0,01602
Lack of Fit	3	0,647519	0,21584	50,43	0,001233	0,015607
Pure Error	4	1,71E-02	4,28E-03			0,000413

Table 6.16
ANOVA report of NCSS for the third set of experiments

ANOVA Section						
		Last	Mean		Prob	Term
Factor	df	Sum-Squares	Square	F-Ratio	Level	R-Squared
C1	3	38,31796	12,77265	134,52	0,000001	0,923592
C2	3	5,322392	1,77413	18,69	0,001014	0,128288
Total Error	7	0,664638	0,094948			0,01602
Lack of Fit	3	0,647519	0,21584	50,43	0,001233	0,015607
Pure Error	4	1,71E-02	4,28E-03			0,000413
ANOVA Section Using Pure Error						
		Last	Mean		Prob	Term
Factor	df	Sum-Squares	Square	F-Ratio	Level	R-Squared
C1	3	38,31796	12,77265	2984,37	0	0,923592
C2	3	5,322392	1,77413	414,53	0,000019	0,128288
Total Error	7	0,664638	0,094948			0,01602
Lack of Fit	3	0,647519	0,21584	50,43	0,001233	0,015607
Pure Error	4	1,71E-02	4,28E-03			0,000413

Table 6.17
Estimation report of NCSS for the third set of experiments

Estimation Section						
		Regression	Standard		Prob	Last
Parameter	df	Coefficient	Error	T-Ratio	Level	R-Squared
Intercept	1	3,40582				
C1	1	92,01608	13,35356	6,89	0,000233	0,108667
C2	1	-1,04336	1,552325	-0,67	0,52306	0,001034
C1^2	1	-518,028	46,93144	-11,04	0,000011	0,278833
C2^2	1	-1,05473	0,469314	-2,25	0,059427	0,011559
C1*C2	1	31,02	6,162736	5,03	0,001507	0,057983
Model						
3.40582+ 92.01608*C1-1.043361*C2-518.0278*C1^2-1.054731*C2^2+ 31.02*C1*C2						
Estimation Section Using Pure Error						
		Regression	Standard		Prob	Last
Parameter	df	Coefficient	Error	T-Ratio	Level	R-Squared
Intercept	1	3,40582				
C1	1	92,01608	2,835096	32,46	0,000005	0,108667
C2	1	-1,04336	0,329574	-3,17	0,033995	0,001034
C1^2	1	-518,028	9,964022	-51,99	0,000001	0,278833
C2^2	1	-1,05473	9,96E-02	-10,59	0,000451	0,011559
C1*C2	1	31,02	1,308412	23,71	0,000019	0,057983
Model						
3.40582+ 92.01608*C1-1.043361*C2-518.0278*C1^2-1.054731*C2^2+ 31.02*C1*C2						

Table 6.18
Optimum Solution report of NCSS for the third set of experiments

Optimum Solution Section		
	Maximum	Optimum
Parameter	Exponent	Value
C1	2	0,132218
C2	2	1,449675
Function at optimum	8,732635	
Number of Function Evaluations	396	
Maximum Functions Evaluations	500	

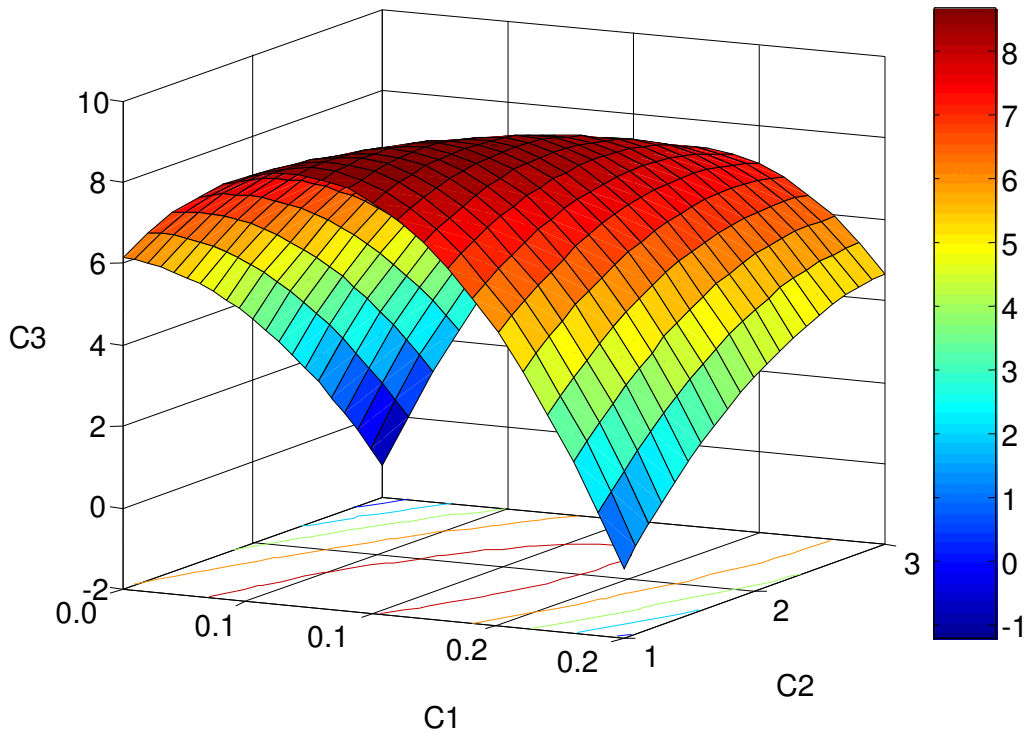

Figure 6.6 Response Surface Plot of C3 for the third set of experiments

6.5 Comparison of the Experiments

Looking at Table 6.18, we see that our optimum values found by NCSS are between the interval values for the first time, and the response is estimated as 8.732, which is the highest value NCSS estimated. The intervals we have chosen also covered all the commercially used collimators for our purpose, which is why we put an end to our experiments. Then, we simulate the optimum values with SIMIND; compute the outputs of SIMIND with MATLAB to see the experimental results. This is for the validation of the estimated results.

Table 6.19
Comparison of NCSS and SIMIND calculations SNR values for the optimums

Optimal Values for hole diameter & hole length				
	Hole Diameter	Hole Length	Estimation of NCSS	SNR results of SIMIND
1	0,195	1,413	8,2106	7,9922
2	0,095	1,532	8,5296	7,9407
3	0,132	1,449	8,7326	8,6061

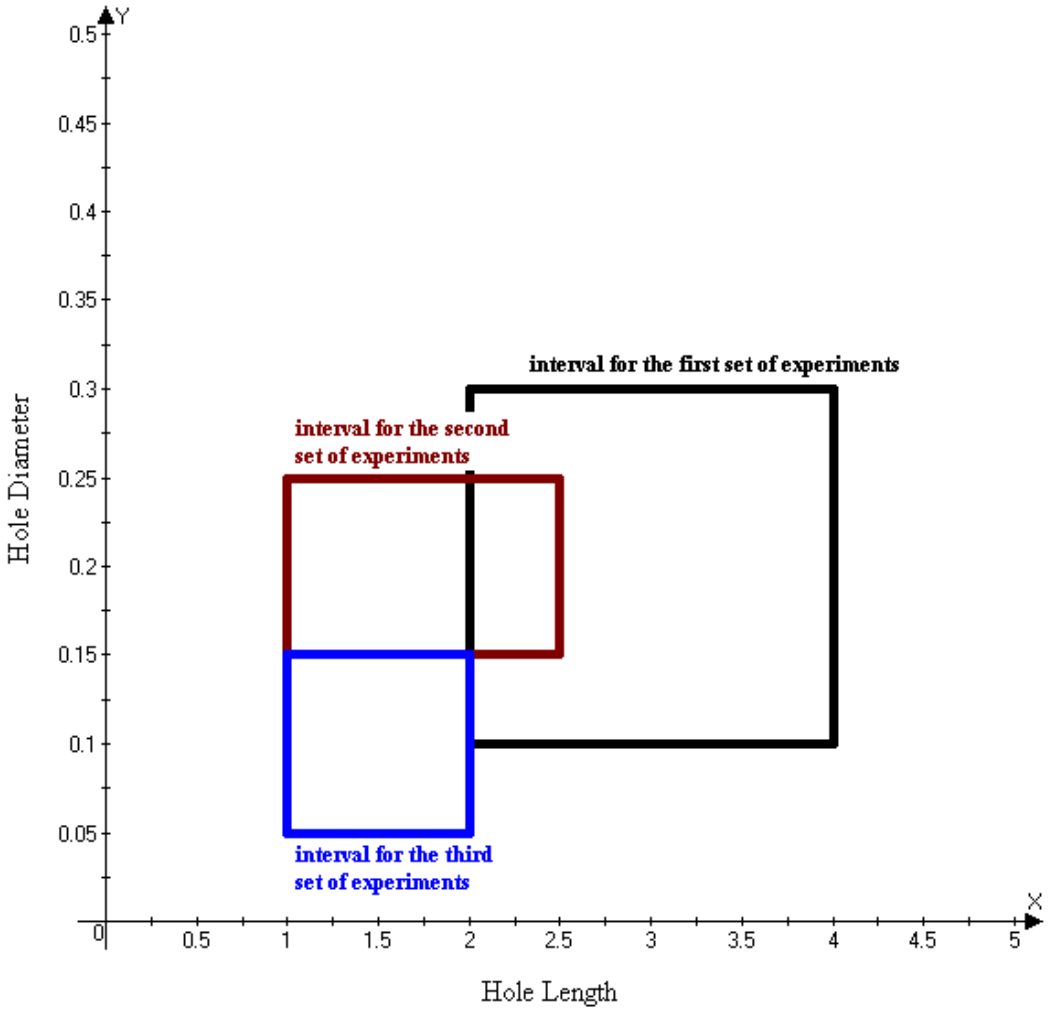

Figure 6.7 Interval values for the experiments

We see in Table 6.19 that the optimum values for the third set of experiments give the best results of SNR in the simulation studies. Moreover, estimated SNR value of the third set of experiments has the least error compared to the simulation SNR result. We can have a better understanding of these optimum values by looking at the profiles, which are the outputs of the MATLAB program. The optimum values of the first collimator have the most number of counts because of the large hole diameter but they lack resolution because of the bad distribution seen at the x-axis (Figure 6.6). With the second collimator, we have better distribution but number of counts is reduced to half thus the sensitivity decreased (Figure 6.7). The optimum values of the last collimator obtain nearly the same resolution as the second one but also the number of

counts increases (Figure 6.8). The number of counts is not as much as the first one but a trade off between resolution and sensitivity is obtained as well as the highest SNR value.

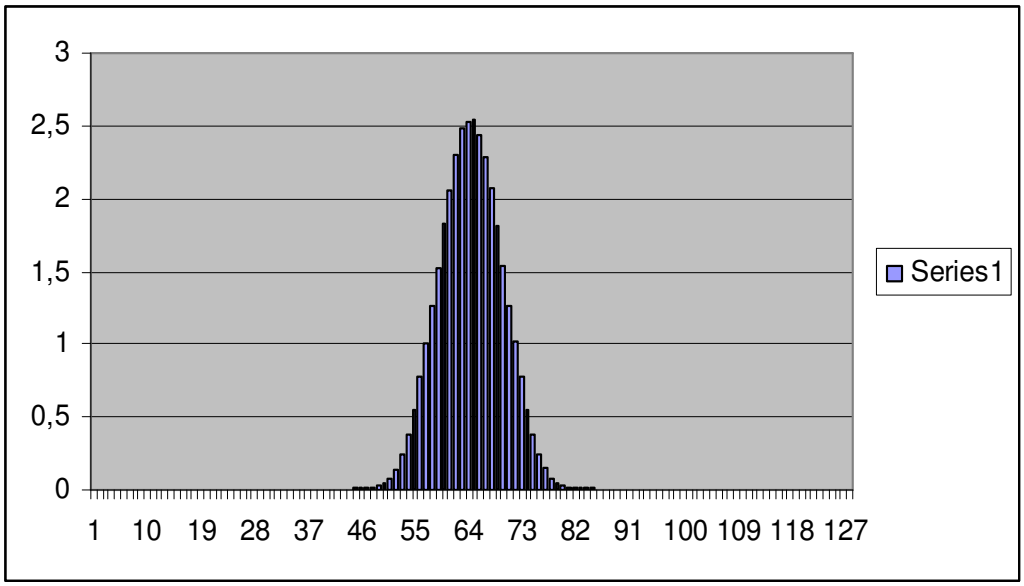

Figure 6.8 Profile for the optimum values of the first set of experiments, where the hole diameter is 0.195cm and the hole length is 1.413cm

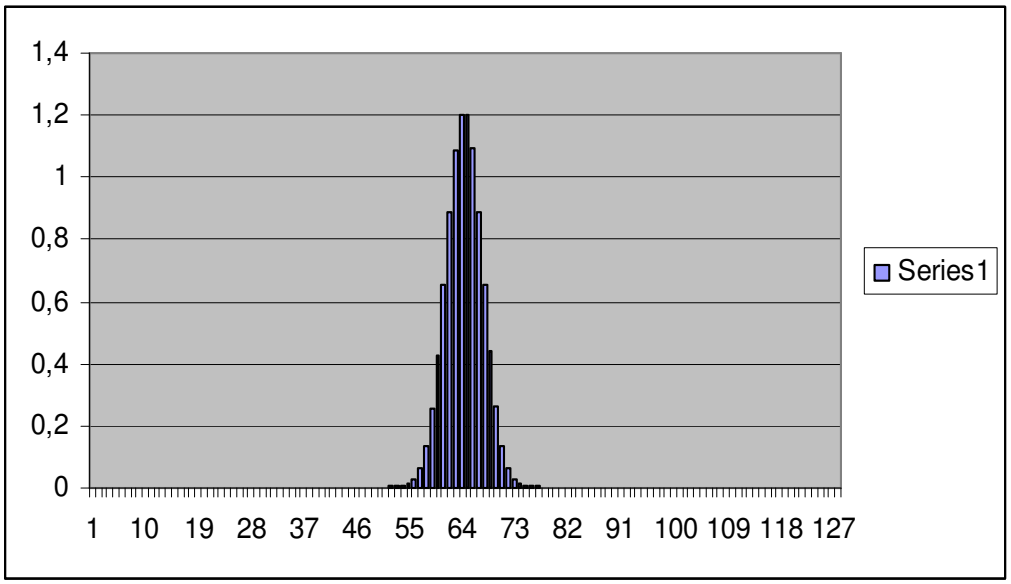

Figure 6.9 Profile for the optimum values of the second set of experiments, where the hole diameter is 0.095cm and the holelength is 1.532cm

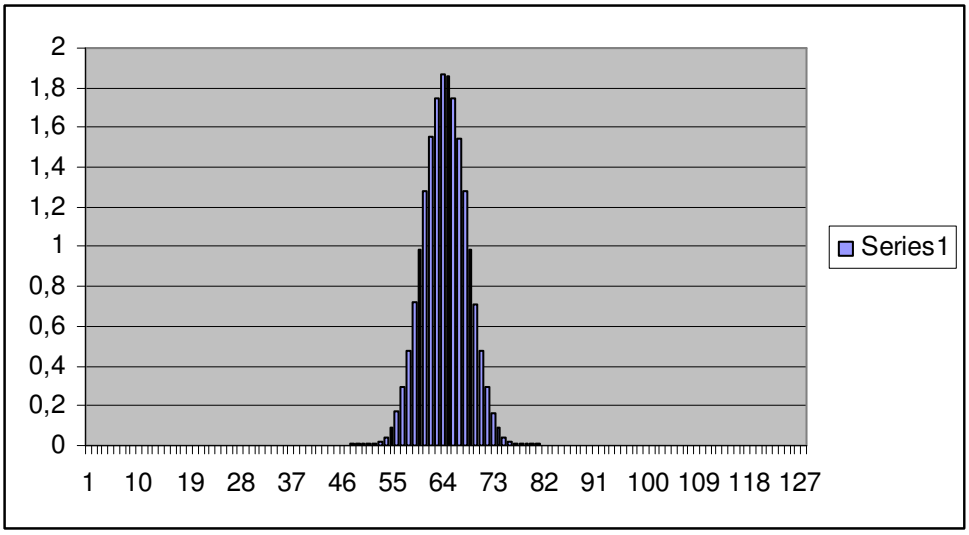

Figure 6.10 Profile for the optimum values of the third set of experiments, where the hole diameter is 0.132cm and the hole length is 1.449cm

6.6 Comparison with the Commercial Collimators

We have simulated some of the commercially used collimators to see their SNRs (Table 6.20). These collimators are: General Electric's GE-LEGP (Low Energy General Purpose), Engineering Dynamics Corporation's ED-LEUR (Low Energy Ultra-High Resolution) and ED-LEHR (Low Energy High Resolution), Von Gahlen Collimators' VG-LEHR and VG-LEUR, Simens' SI-LEAP (Low Energy All Purpose) and SI-LEHR. Optimum is the optimized collimator we have reached in the end of the third set of experiments. In Table 6.20 we can see that according to the SNR criteria Optimum has the best ranking among the commercially used collimators. Another thing that attracts attention is that Optimum has the lowest hole length size.

Table 6.20
Ranking of different collimator sizes by SNR

Collimator	Rank	Hole Diameter	Septa	Hole Length	SNR
GE-LEGP	7	0,250	0,030	4,1	6,7835
ED-LEUR	5	0,140	0,018	2,920	7,0276
ED-LEHR	3	0,140	0,020	2,540	7,5335
VG-LEHR	6	0,170	0,020	3,500	6,9278
VG-LEUR	8	0,130	0,020	3,500	5,9643
SI-LEAP	2	0,145	0,020	2,410	7,8160
SI-LEHR	4	0,111	0,016	2,360	7,1907
Optimum	1	0,132	0,020	1,449	8,6061

7. CONCLUSION

The goal of this thesis was to find the optimum sizes of the hole diameter and the hole length of a parallel-hole collimator for breast scintigraphy. SIMIND was used to simulate the gamma camera system and to carry out the experiments. SNR was used as a detectability index and a MATLAB program was developed to find SNR values from the outputs of SIMIND. RSM method was used for the optimizing process, which has not been used in nuclear era before.

Optimum values that we have found do not match some of the other works of collimator optimization in literature. For example, Gengsheng L. Zeng et. al. and Grant T. Gullberg et. al. [8] found the optimum value for the hole diameter as 0.366cm but it should be noted that in their work only the hole diameter was a variable. On the other hand, G.H. Simmons et. al. [4] found the optimum hole diameter value of a parallel-hole collimator as 0.200cm but again only the hole diameter was a variable.

The hole diameter and hole length sizes of commercial collimators range from 0.15cm to 0.30cm and 2.00cm to 5.00cm according to the purpose of the collimator as well as the manufacturer. The optimum size we have found for the hole diameter seems to match Siemens based collimators but not with General Electric based ones. Hole length size of our optimal collimator is lower then any of the commercially used collimator's while it has better SNR value according to the simulation studies.

For future work, robust design can be investigated to add noise factors to our current design. Robust gives the opportunity to investigate varying lesion position and size and thus may give more accurate results. Moreover, a collimator with the optimum parameters can be manufactured to do physical experiments.

APPENDIX A. MATLAB PROGRAM

```
%detectability with other indices%
clear
close all
fid=fopen('*.BIM');
[AA]=fread(fid,[128,128],'single');
status = fclose(fid);
fid=fopen('*.BIM');
[BB]=fread(fid,[128,128],'single');
status = fclose(fid);
whos
a1=128;
a2=128;
pbtotal=0;
ps2total=0;
ps22total=0;
pbtot=0;
pstot=0;
%cons=acquisition time in seconds%
cons=600;
ij=0;
for i=5:100
  for j=5:100
       BBB=double(BB(i,j));
       BBB=cons*BBB;
       ps22total=ps22total;
       ps22total=ps22total+BBB^2;
    if (i-64.5)^2+(j-64.5)^2 <= 9
ps2total=ps2total+BBB^2; ij=ij+1; pstot=pstot+cons*BB(i,j);
pbtot=pbtot+cons*AA(i,j); end
 end
```

```
ps2total
ps2sqrt=sqrt(ps2total)
ps22sqrt=sqrt(ps22total)
psmean=pstot/ij
for i=63:65
  for j=63:65
    AAA=double(AA(i,j))
    pbtotal=pbtotal+cons*AAA;
    BBB=double(BB(i,j))
  end
end
pbmean=pbtotal/9
pbmeans=sqrt(pbmean)
d=ps2sqrt/pbmeans
d2=ps22sqrt/pbmeans
contrast=psmean/pbmean
percentagesd=pbmeans/pbmean
SNR=contrast/percentagesd
CC=10*double(AA)+10*double(BB);
WK1WRITE('EXCEL1',BB)
```

REFERENCES

1. Richard, C. Cho, Iraj Khalkhali, Gregory, M., Eckel, *A Vision for Nuclear Imaging in Breast Cancer Care, Department of Radiology*, LA BioMed Research Institute at Harbor-UCLA Medical Center.
2. Buvat, I., S. Laffont, Cloirec, J.L., P. Bourget, and Paola, R.D., "Importance of the choice of the collimator for the detection of small lesions in scintimammography: a pantom study," *Physics in Medicine and Biology,* Vol.46, pp.1343-1355, 2001.
3. Simmons, G.H., *A Non-linear Programming Method for Optimizing Parallel-hole Collimator Design*, Bureau of Radiological Health, FDA and Department of Radiology, University of Cincinnati College of Medicine
4. Zeng, L., Gengsheng, and Grant T. Gullberg, "A channelized-hotelling-trace collimator design method based on reconstruction rather than projections," *IEEE Transactions on Nuclear Science*, Vol. 49, pp.2155-2158, 2002.
5. Sain, J.D., and Barrett, H.H., "Performance evaluation of a modular gamma camera using a detectability index," *The Journal of Nuclear Medicine*, Vol.44, pp.58-66, 2003.
6. Bombardieri, E., Cumali Aktolun, Baum, P., Richard, Angelika Bishof-Delaloye, John Buscombe, Jean Francois Chatal, Lorenzo Maffioli, Roy Moncayo, Luc Mortelmans, Sven N. Reske, "Breast scintigraphy: procedure guidelines for tumour imaging," *Eur J Nucl Med Mol Imaging*, Vol.23, pp.609-611, 2003.
7. Mankoff, D., "Imaging in Breast Cancer – Breast Cancer Imaging Revisited", *Breast Cancer Research*, Vol.7, pp.276-278, 2005.
8. http://www.nuclear.kth.se/courses/medphys/5A1414/GC-labb.pdf
9. Jonasson, T., *Revival of a Gamma Camera*, Nuclear Physics Group Physics Department Royal Institute of Technology, Master of Science Thesis, 2003.
10. Sprawls, P., *Physical Principles of Medical Imaging*, Aspen Publications, Rockville, 1987.
11. *Introduction to Monte Carlo Methods*, by the Computational Science Education Project (CSEP), available at: http://www.cse.psu.edu/~raghavan/cse557/MC.pdf
12. Zaidi, Habib, "Monte Carlo Techniques in Diagnostic and Therapeutic Nuclear Medicine", Standards and Codes of Practice in Medical Radiation Dosimetry, ISBN 92-0-111403-6 *Proc. of an International Symposium*, Vol.2, pp.29-44, 2002.
13. Ljungberg, M., Strand, S.E., and King, M. A. *Monte Carlo Calculation in Nuclear Medicine: Applications in Diagnostic Imaging,* IOP Publishing, Bristol and Philadelphia, pp.145-163, 1998.
14. Zaidi, H., "Relevance of accurate Monte Carlo modeling in nuclear medical imaging," *Med Phys* Vol.26, pp.574-608, 1999.
15. Ljungberg M., S. Strand, "A Monte Carlo program for the simulation of scintillation camera characteristics," *Computer Methods and Programs in Biomedicine,* Vol.29, pp.257-272, 1989.

16. Dewaraja, Y. K., Ljungberg, M., and Koral, K. F. "Characterization of scatter and penetration using Monte Carlo simulation in 131-I imaging," *J.Nucl.Med.* Vol.41, pp.123-130, 2000.

17. The SIMIND Monte Carlo program (Available at): http://www.radfys.lu.se/simind/Downloads.html

18. Freifelder, Richard, and Joel S Karp, "Dedicated PET scanners for breast imaging," *Phys. Med. Biol.* Vol.42, pp. 2463-2480, 1997.

19. Cosman, C. Pamela, Robert M. Gray, Olsen, A., Richard, "Evaluating quality of compressed medical images: SNR, subjective rating, and diagnostic accuracy," *Proceedings of the IEEE*, Vol. 82, pp.919-932, June 1994.

20. Loo L. N., Doi K., and Metz C. E. "A comparison of physical image quality indices and observer performance in the radiographic detection of nylon beads," *Phys. Med. Biol.* Vol.29, pp.837-56, 1984.

21. Barrett, H., Harrison, Jie Yao, Rollandt, P., Jannick, Kyle J. Myerst, "Model observers for assessment of image quality," *Proc. Natl. Acad. Sci.* USA Vol. 90, pp. 9758-9765, 1993.

22. Montgomery, C., Douglas, *Design and Analysis of Experiments: Response Surface Methods,* Jon Wiley&Sons, New York, 2004.

23. Sanchez, M., S., "Robust design," *Proceedings of the 26th Winter Simulation Conference*, pp.106-113, 1994.

24. Welch, W. J., T. K. Yu, S. M. Kang, and J. Sacks. "Computer experiments for quality control by robust design," *Journal of Quality Technology,* Vol.22, pp.15–22 1990.